PHYSICAL REVIEW FLUIDS **6**, 013602 (2021)

Numerical study of the interaction between a pulsating coated microbubble and a rigid wall. II. Trapped pulsation

M. Vlachomitrou [*] and N. Pelekasis [†]
Department of Mechanical Engineering, University of Thessaly, Leoforos Athinon,
Pedion Areos, 38834 Volos, Greece

(Received 16 March 2020; accepted 4 December 2020; published 6 January 2021)

The dynamic response of an encapsulated bubble subject to an acoustic disturbance in a wall restricted flow is investigated, when the viscous forces of the surrounding liquid are accounted for. The Galerkin finite element methodology is employed and the elliptic mesh generation technique is used for updating the mesh. As the bubble accelerates towards the wall, the dominant force balance is between Bjerknes forces and the viscous drag that develops. In this process a prolate shape is acquired by the bubble, due to excessive compression at the equator region. When the bubble reaches the wall lubrication pressure develops in the near wall region that resists further approach. As long as the sound amplitude remains below a threshold value determined by the onset of parametric shape mode excitation saturated, or “trapped,” pulsations are performed around a certain small distance from the wall. The balance between Bjerknes attraction and the lubrication pressure that arises due to shell bending along the flattened shell portion that faces the wall generates an oblate shape. Elongation is now observed along the equatorial plane where a local liquid overpressure is established generating large tensile strain. The time-averaged deflection of the microbubble at the pole that lies close to the wall is determined by the bending and stretching resistances of the shell in the manner described by Reissner’s linear law for a static compressive load on an elastic shell, corrected for the effect of surface tension. The oscillatory part of the bubble motion in that same region, the contact region, follows the forcing frequency and consists of a pressure driven and a shear flow in the form of a Stokes layer where a significant amount of instantaneous wall shear is generated. The thickness of the film that occupies the Stokes layer is on the order of a few tenths of nm and is determined by the balance between liquid and shell tangential viscous stresses. The steady streaming effect on the wall shear is absent owing to the negligible phase difference between the volume and center of mass pulsations.

DOI: 10.1103/PhysRevFluids.6.013602

I. INTRODUCTION

The dynamic behavior of encapsulated microbubbles, also known as contrast agents, plays a key role in novel biomedical applications involving ultrasound among which the most important are medical imaging of vital organs and targeted drug delivery. In the former case, gas-filled microbubbles are used which are able to enhance the ultrasound backscatter and contrast, in comparison with the acoustic signal from nearby tissue, thus producing high quality images [1] as a result of their nonlinear nature as sound scatterers [2]. Targeted molecular imaging has also been developed [3], whereby specific ligands are attached to the membrane to facilitate the adhesion of

---

[*] mavlacho@uth.gr
[†] pel@uth.gr

the microbubble to a specific diseased area in order to provide better contrast enhancement. In a similar fashion, in targeted drug delivery encapsulated microbubbles that carry drugs are attached to the affected site using an appropriate acoustic disturbance and then ruptured via sonication. Alternatively, low amplitude oscillations of coated microbubbles are employed for the transport of large macromolecules towards the cell cytoplasm via generation of transient micropores in nearby cells [4,5] or via the acoustic microstreaming process [6,7]. In both situations it is essential to resolve the details of the flow that develops in the region between the wall and the bubble shell.

For such flow arrangements experimental studies report that the presence of a nearby boundary accelerates growth of interfacial instabilities and instigates phenomena like jet formation and, finally, collapse of the bubble [8,9]. The latter experimental studies examine the situation with the coated microbubble pulsating in response to an acoustic disturbance in the vicinity of a boundary. In this fashion microbubble shapes that are asymmetrically deformed in the direction perpendicular to the boundary surface, alternating between the prolate and oblate configuration, were captured [8] while jet formation was observed in the compression [10] and expansion phase of the pulsation [9], respectively. In a different context, Garbin *et al.* [11] studied the effect of the secondary acoustic radiation force to the translational dynamics of contrast agents that are in contact with or adhered to a semirigid membrane. They found that there is a critical threshold beyond which secondary acoustic radiation force can cause the detachment of adherent bubbles. In an ensuing study [12] it was observed that targeted microbubbles that are attached to an underlying surface and subject to secondary Bjerknes forces due to a neighboring trapped microbubble tend towards a prolate shape along the line connecting the two bubbles, whereas for higher acoustic pressures secondary Bjerknes forces disrupt the molecular adhesion of the bubble to the surface. It was thus proposed that acoustic radiation forces may be employed as a means to measure the strength of adhesion forces between coated microbubbles and various substrates.

Furthermore, in applications of targeted drug delivery and sonoporation, trapping of the microbubble on the nearby tissue and the ensuing pulsations it performs are crucial factors of the efficiency of the overall process and are expected to be significantly affected by the interplay between Bjerknes, lubrication, and adhesion forces. In particular, they are of central importance in identifying the acoustic signature of freely circulating and trapped microbubbles and assessing the potential for sonoporation to take place. In fact, Marmottant and Hilgenfeldt [6], based on a previous study by Longuet-Higgins [13] for small streaming Reynolds, showed that when the amplitude of the radial motion of the bubble is taken to be smaller than the dimensionless boundary layer thickness around the bubble, a strong streaming motion away from the wall develops, provided the radial and translational pulsations appear with a significant phase lag. Doinikov and Bouakaz [7] identified interaction between the rotational and irrotational part of the motion as the controlling step for the onset of acoustic microstreaming, and the wall presence was seen to strongly influence the intensity of acoustic streaming near the wall due to a pulsating bubble that remains at a large distance from it, in comparison with the bubble radius. In a more recent study Mobadersany and Sarkar [14] extended the previous study by Doinikov and Bouakaz [7] to capture acoustic streaming for the case of a contrast agent that pulsates next to a rigid wall. It is of interest to place our results and examine their validity in the context of the above theoretical studies.

It should be stressed that extensive numerical simulations of the dynamic response of contrast agents are not available in the literature, owing largely to uncertainties regarding proper modeling of the shell, especially in the case of phospholipid shells. Furthermore, the degree to which potential flow considerations can sufficiently capture the dynamic behavior of deforming contrast agents is not fully understood [15]. Qin and Ferrara [16] developed a lumped parameter model as a means to incorporate elastic effects, mainly in the surrounding vessel, in order to study the acoustic response of a coated microbubble that pulsates in a compliant microvessel. They were thus able to calculate the stresses that develop on the microvessel wall as result of the pulsating motion, which was also seen to increase the permeability of the vessel. More recently, numerical studies were conducted to address the above issues via the finite volume [17] and boundary integral method [15] as a means to obtain a more detailed description of the velocity field in the surrounding fluid. In this fashion, harmonic and subharmonic shape mode excitation was obtained in agreement with previous predictions based on linear stability analysis [18]. Furthermore, boundary integral simulations of pulsating contrast agents [15], ignoring viscous effects on the liquid side in view of the relatively large shell viscosity and the typical small size of encapsulated bubbles, recovered harmonic and subharmonic shape mode excitation that led to saturated shape oscillations or breakup beyond a certain amplitude threshold. In the present study we numerically investigate the dynamic response of a contrast agent to an acoustic disturbance in a wall restricted flow when the viscous forces of the surrounding liquid are accounted for, and we focus on identifying the mechanism that facilitates and controls the trapping procedure. Emphasis is placed on illustrating the interplay between secondary Bjerknes forces, lubrication pressure, and viscoelastic shell stresses in establishing a steady pulsation of a trapped microbubble and obtaining conditions for such a dynamic state to be achieved. The effect of adhesion on the substrate in the form of an interaction potential, attractive or repulsive, is left for a future study due to the additional numerical challenge it poses as a result of the different length scales involved in modeling such flow arrangements.

The material presented in this paper is organized as follows: The problem formulation is discussed in Sec. II, where the governing equations for the liquid flow are presented along with the ones describing the encapsulated bubble. Next, in Sec. III the numerical method that has been developed for discretizing the governing equations, as well as the grid construction procedure, are briefly outlined as they are presented in full detail in [19,20]. The latter reference, i.e., [20], that treats the initial stages of the motion of the microbubble towards the wall before the dynamic state of saturated pulsations is established, will be referred to as paper I hereinafter. In Sec. IV the results of our simulations are presented as the bubble performs trapped pulsations and the potential for the onset of acoustic streaming is examined and discussed in the context of previous studies. Finally, in Sec. V the main conclusions are summarized and directions for future research are outlined.

II. PROBLEM FORMULATION

We are interested in examining the dynamic response to acoustic disturbances of an encapsulated microbubble in a wall restricted flow. In particular we want to focus on the late stages of its motion towards the wall during which the microbubble performs saturated pulsations, trapped pulsations, in the vicinity of the wall and wish to define conditions that lead to this dynamic state. To this end we follow the dynamics of a microbubble with initial radius R_0 that is submerged in a Newtonian liquid of density ρ and dynamic viscosity μ. We consider a wall-restricted flow by placing the bubble at a certain initial distance from the wall and we investigate the bubble's response to an acoustic disturbance imposed on the far field pressure:

$$P'_\infty = P'_{\text{st}} + P'_{\text{dist}} = P'_{\text{st}} + P'_{\text{st}}\varepsilon\cos(\omega_f t') \tag{1}$$

with P'_{st}, P'_{dist} denoting the dimensional undisturbed and disturbed pressure in the far field, respectively, ε the magnitude, and ω_f the angular velocity of the imposed disturbance. The initial radius R_0 of the bubble is taken as the characteristic length scale of the problem, whereas the external frequency determines the appropriate time scale as $1/\omega_f$. Therefore, the characteristic velocity and pressure scales are $\omega_f R_0$ and $\rho\omega_f^2 R_0^2$, respectively. Throughout this paper primed letters signify dimensional variables, in the manner presented in paper I.

In order to obtain the governing equations we consider a cylindrical coordinate system and assume axisymmetric variations of the bubble shape as well as the liquid velocity and pressure. In Fig. 1 a schematic representation of the flow under consideration is provided with f_1 denoting the r coordinate of the thin shell that coats the bubble.

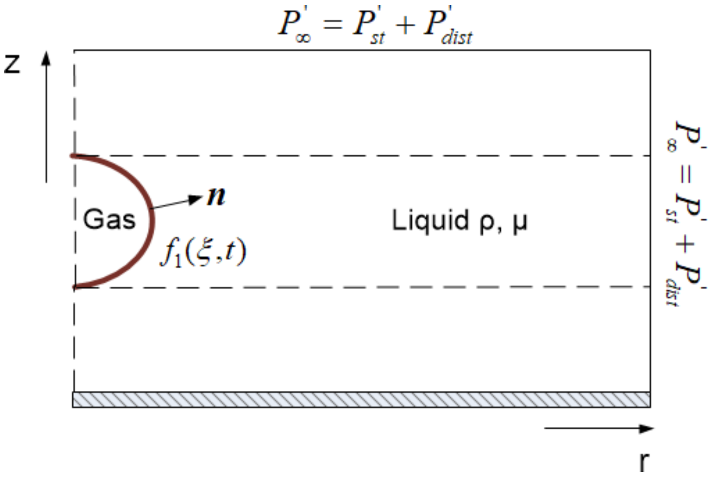

FIG. 1. A contrast agent in a wall-restricted flow.

The flow in the surrounding liquid is governed by the mass conservation and momentum equations. The liquid is taken to be incompressible in which case the continuity equation and momentum balance, via the Navier-Stokes equations, read in dimensionless form:

$$\nabla \cdot \boldsymbol{u} = 0, \tag{2}$$

$$\frac{\partial \boldsymbol{u}}{\partial t} + (\boldsymbol{u} \cdot \nabla)\boldsymbol{u} = -\nabla P + \frac{1}{\mathrm{Re}} \nabla \cdot \underline{\underline{\boldsymbol{\tau}}}, \quad \underline{\underline{\boldsymbol{\sigma}}} = -P\underline{\underline{\boldsymbol{I}}} + \frac{1}{\mathrm{Re}}\underline{\underline{\boldsymbol{\tau}}}, \quad \underline{\underline{\boldsymbol{\tau}}} = \nabla \boldsymbol{u} + \nabla \boldsymbol{u}^T, \tag{3}$$

where $\boldsymbol{u} = (u_r, u_z, 0)$ for the cylindrical coordinate system, $\mathrm{Re} = (\rho \omega_f R_0^2)/\mu$ is the Reynolds number pertaining to the radial component of the surrounding liquid flow that compares inertia with viscous forces, $\underline{\underline{\boldsymbol{\sigma}}}$, $\underline{\underline{\boldsymbol{\tau}}}$ are the full and deviatoric stress tensors in the surrounding fluid, and $\underline{\underline{\boldsymbol{I}}}$ is the unit tensor. In the above formulation buoyancy has been neglected owing to the small size of the bubbles and the flow is treated as incompressible. In order to obtain the deformation of the bubble we use a Lagrangian representation of the interface by introducing a Lagrangian coordinate ξ $(0 \leqslant \xi \leqslant 1)$ which identifies the particles on the interface with $\xi = 0$ and $\xi = 1$ corresponding to the south and north pole of the bubble respectively.

The force balance on the gas-liquid interface reads in dimensionless form

$$\left(-P\underline{\underline{\boldsymbol{I}}} + \frac{1}{\mathrm{Re}}\underline{\underline{\boldsymbol{\tau}}}\right) \cdot \boldsymbol{n} + P_G \boldsymbol{n} = \frac{(\nabla_s \cdot \boldsymbol{n})\boldsymbol{n}}{\mathrm{We}} + \boldsymbol{\Delta F} = \frac{2k_m}{\mathrm{We}}\boldsymbol{n} + \boldsymbol{\Delta F}, \tag{4}$$

where $\boldsymbol{n}$ denotes the unit normal vector pointing towards the surrounding fluid, P_G is the pressure of the gas inside the bubble, ∇_s, k_m denote the surface gradient and mean curvature of the bubble's interface, respectively, and $\mathrm{We} = \frac{\rho \omega_f^2 R_0^3}{\sigma}$ is the Weber number comparing inertia with capillary forces. Despite its viscoelastic nature a certain amount of surface tension σ is typically assumed for the shell [20–24], as a measure of the isotropic surface tension that signifies the macroscopic effect of regions on the shell where direct contact between the enclosed gas and the surrounding liquid exists. Finally, $\boldsymbol{\Delta F}$ is the resultant force due to the viscoelastic properties of the membrane. Based on the theory of elastic shells [25,26] the resultant force $\boldsymbol{\Delta F}$ in the case of a contrast agent is derived by the surface divergence of the viscoelastic tension tensor on the membrane surface and is equal to

$$\boldsymbol{\Delta F} = \left[k_s \tau_s + k_\phi \tau_\phi - \frac{1}{r}\frac{\partial}{\partial S}(rq)\right]\boldsymbol{n} - \left[\frac{\partial \tau_s}{\partial S} + \frac{1}{r}\frac{\partial r}{\partial S}(\tau_s - \tau_\phi) + k_s q\right]\boldsymbol{e}_s \tag{5}$$

with S denoting the arclength of the interface, τ_s, τ_ϕ the principal elastic tensions, k_s, k_ϕ the two principal curvatures, r, z the cylindrical polar and axial coordinates, and $\boldsymbol{e}_s$ the tangential unit vector; q denotes the transverse shear tension that is obtained from a torque balance on the shell [25,26]:

$$q = \frac{K_B}{r}\frac{\partial r}{\partial S}\left[\frac{\partial}{\partial r}(r m_s) - m_\phi\right], \tag{6a}$$

where m_s, m_ϕ are the principal bending moments and $K_B \equiv k_B/(\rho\omega_f^2 R_0^5)$ signifies the relative importance of bending with respect to inertia. The membrane and bending stresses are defined via the shell constitutive laws. In particular, the transverse shear q points along the normal vector $\boldsymbol{n}$ of a surface that is perpendicular to the tangent vector $\boldsymbol{e}_s$. Finally, the membrane tensions consist of an elastic and a viscous component, i.e.,

$$\tau_s = \tau_{s,\mathrm{el}} + \tau_{s,v}, \quad \tau_s^{\mathrm{MR}} = \frac{G}{3\lambda_s\lambda_\varphi}\left(\lambda_s^2 - \frac{1}{(\lambda_s\lambda_\varphi)^2}\right)\left[1 + b\left(\lambda_\varphi^2 - 1\right)\right] + \frac{2}{\mathrm{Re}_s}\frac{1}{\lambda_s}\frac{\partial\lambda_s}{\partial t}, \tag{6b}$$

$$\lambda_s = \frac{S_\xi(t)}{S_\xi(0)}, \quad \lambda_\phi = \frac{r(t)}{r(0)} \tag{6c}$$

with λ_s, λ_φ denoting the principal extension ratios and $G \equiv \chi/\rho\omega_f^2 R_0^3$ and $\mathrm{Re}_s \equiv \rho\omega_f R_0^3/\mu_s$ signifying the relative importance of shell dilatation and viscosity with respect to inertia. We adopt the Mooney Rivlin model for the elastic part with b denoting the degree of shell softness [27] and a linear model for shell viscosity μ_s treating the dilatational and shear viscosity of the shell as equal.

A more detailed description of the modeling that is used for the force balance on the viscoelastic shell that coats the bubble is given in Tsiglifis and Pelekasis [15,18,21] and Vlachomitrou and Pelekasis [19,20] as well as in paper I, based on previous theoretical treatments in [25,26].

Besides the force balance, the continuity of the liquid and shell velocities on the interface reads as

$$\boldsymbol{u} = \frac{D\boldsymbol{r}_s}{Dt} \tag{7}$$

with $\boldsymbol{r}_s = r\boldsymbol{e}_r + z\boldsymbol{e}_z$ denoting the position vector of a particle at the interface. At equilibrium a stress free state is assumed on the interface of radius R_0, where the dimensionless pressure P_G inside the bubble is related to the dimensionless pressure P_{st} on the far field through the Young-Laplace equation:

$$P_G(t=0) = P_{\mathrm{st}} + \frac{2}{\mathrm{We}}. \tag{8}$$

The pressure inside the bubble is taken to be uniform due to negligible density and kinematic viscosity of the enclosed gas. Moreover, heat transfer between the bubble and the surrounding liquid is assumed to take place quite fast, in comparison with the time scale of the phenomena under consideration. In this context, bubble oscillations are characterized as nearly isothermal and therefore the bubble pressure is given by

$$P_G(t=0)V_G^\gamma(t=0) = P_G(t)V_G^\gamma(t) \tag{9}$$

with V_G denoting the dimensionless instantaneous volume of the bubble, $V_G(t=0) = \frac{4\pi}{3}$ the initial volume of the bubble, and γ the polytropic constant set to 1.07 for an almost isothermal variation. The latter value is also close to the ratio between the specific heats of certain ideal gases that are carried by known contrast agents and undergo adiabatic pulsations during insonation [21,23,24].

III. NUMERICAL METHODOLOGY

A detailed description of the numerical methodology that is used to simulate the dynamic behavior of a contrast agent when the viscous forces of the surrounding liquid are accounted for

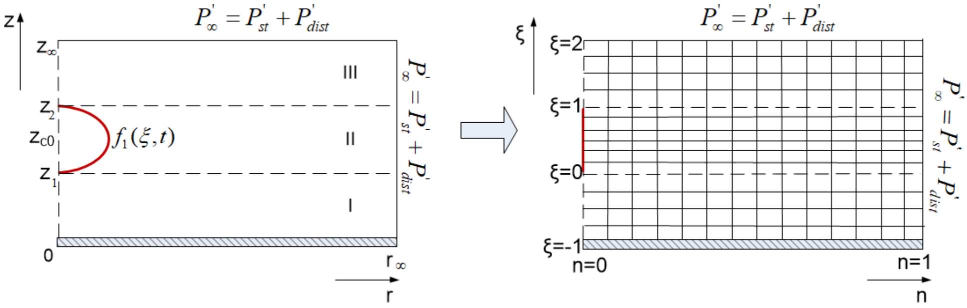

FIG. 2. Schematic representation of the physical and the computational domain for the case of a bubble in wall restricted flow.

is provided in Vlachomitrou and Pelekasis [19] for an unbounded flow and in paper I where the numerical methodology is extended in order to take into account wall presence. The numerical solution is performed via a superparametric Galerkin finite element methodology with a hybrid scheme that uses two-dimensional (2D) Lagrangian functions to discretize the surrounding flow field, in conjunction with 1D cubic splines for the bubble shape. In the case of an encapsulated bubble the introduction of cubic splines is necessary because a fourth order derivative arises in the force balance equation through the bending resistance of the membrane. More specifically, biquadratic and bilinear Lagrangian basis functions are used for the velocity and the pressure of the liquid, respectively, while cubic spline functions are employed to discretize the interface. The continuity of the radial and axial velocity components is imposed as an essential boundary condition on the interface. Furthermore, since we employ a Lagrangian representation for the shape of the bubble we need two equations for each particle ξ to determine the two coordinates $r(\xi,t)$ and $z(\xi,t)$. For this reason the normal and tangential force balances are employed and are discretized using the one dimensional cubic splines as bases functions [19,20]. In this fashion, discretization of the interfacial force balance equations is facilitated as they contain fourth order derivatives in the form of the bending stresses, with the spline functions interpolating the radial and azimuthal coordinates of the microbubble. With this methodology we are able to simultaneously solve for the velocity and pressure fields along with the shape of the interface. Subsequently, the resulting shape is used as an essential condition to construct the mesh.

Finally, on the far field the imposed pressure disturbance is prescribed, while the velocity components are set to zero. In all simulations presented in this paper the far field was considered to be ten rest radii away from the bubble centroid. In order to ensure the validity of the velocity boundary condition on the outer edge we also performed simulations for larger distances as well that led to the same results.

The nonlinearity of the problem is treated with the Newton-Raphson method, while the fully implicit Euler time integration scheme is introduced in order to make optimal use of its numerical dissipation properties against growth of short wave instabilities. As an overall numerical procedure, at each time step the numerical solution is performed in two stages. In the first stage a Newton-Raphson method is applied in order to solve simultaneously for the velocity and pressure fields along with the shape of the interface. In the second stage, a separate Newton-Raphson iterative procedure complements the above time integration process for the implementation of the elliptic mesh generation scheme [28,29] and the construction of the updated grid. In the latter stage the shape of the bubble is already known and is imposed as an essential condition for the solution of the elliptic equations that provide the grid coordinates. The above procedure offers a significant advantage in that it allows for accurate discretization of the bending stresses and use of greater time steps in comparison with the original method. In Fig. 2 a schematic representation of the physical and the computational domain is given.

According to the employed method the coordinates of the grid points in the physical domain are defined by solving the following set of partial differential equations [29,30]:

$$\nabla \cdot \left(\varepsilon_1 \sqrt{\frac{r_\xi^2 + z_\xi^2}{r_\eta^2 + z_\eta^2}} + 1 - \varepsilon_1\right) \nabla \xi = 0, \tag{10}$$

$$\nabla \cdot \nabla \eta = 0, \tag{11}$$

which upon application of the finite element methodology assume the form

$$\iint \left(\varepsilon_1 \sqrt{\frac{r_\xi^2 + z_\xi^2}{r_\eta^2 + z_\eta^2}} + 1 - \varepsilon_1\right) \nabla \xi \cdot \nabla M_i dr dz = 0, \tag{12}$$

$$\iint \nabla \eta \cdot \nabla M_i dr dz = 0, \tag{13}$$

where M_i are the biquadratic Lagrangian basis functions. In the above equations the integral terms that the divergence theorem produces are omitted in order to weakly impose orthogonality of the grid lines in the boundaries. The first equation produces the η curves which must be nearly perpendicular to the interface, whereas the second equation generates the ξ curves which are nearly parallel to the interface and are prescribed so that they follow its deformation. Introduction of the term $\sqrt{\frac{r_\xi^2+z_\xi^2}{r_\eta^2+z_\eta^2}}$ allows the η curves to intersect the interface almost orthogonally, while ε_1 is an empirical parameter that ranges between 0 and 1 and controls the extent of mesh smoothness versus its orthogonality. Its value in each problem is defined by trial and error and in our case is set to 0.1.

Apart from the elliptic transformation, the appropriate boundary conditions must be introduced. In any boundary where the coordinate is known, the corresponding equation for the grid is not written. Instead, the value of the coordinate is imposed as an essential boundary condition. In the boundaries where we need to control the node distribution the penalty method is applied.

The full details regarding the numerical method and the mesh generation procedure as well as the performed benchmark tests and the grid size independency of the results can be found in paper I. In all simulations presented in Sec. IV the time step was set to 0.01, although smaller time steps (up to 0.001) were also tested to ensure the accuracy of the results. As far as the grid is concerned, we used 80–100, 200, and 80–100 elements in regions I–III of z direction respectively, whereas 80–120 elements were employed in the r direction [see Fig. 2(a)]. Regions I–III are defined along the z direction in order to enforce parallelism of the η lines with respect to the wall in the physical domain [20].

IV. RESULTS AND DISCUSSION

In this section we focus on identifying the mechanism that facilitates and controls the trapping procedure of contrast agents. In this context, we investigate the manner in which their response pattern is influenced by the proximity of a rigid wall, the properties of the protective shell, and the acoustic excitation. Regarding shell properties we focus on the response on lipid shells that are characterized by relatively large resistances to bending and volume compression, $k_B/(\chi R_0^2) \approx 0.1,\ P_{\mathrm{st}} R_0/\chi = O(1)$, based on shell characterization studies via static interrogation [31]. Pertaining to the properties of the acoustic disturbance they are selected so that we operate in the high radial, $\mathrm{Re} = \rho \omega_f R_0^2/\mu \gg 1$, and $O(1)$ translational, $\mathrm{Re}_T = \rho U 2R_0/\mu$, Reynolds numbers while remaining below the threshold for shape mode excitation in order to avoid shell destablilization and breakup. In Table I the parameter range investigated in the present study is provided as well as the amplitude thresholds for shape mode excitation for each case, according to stability analysis [18].

TABLE I. Amplitude thresholds for parametric mode excitation as a function of the shell viscoelastic properties and sound amplitude. The microbubble stress free radius is set to $R_0 = 3.6\,\mu$m, the bending resistance to $k_B = 3 \times 10^{-14}$ N m, the interfacial tension σ to 0.051 N/m, and the Poisson ratio to 0.5. Bold ε's indicate critical amplitude thresholds for given set of shell parameters.

χ (N/m)	k_B (N m)	μ_s (kg/s)	f (MHz)	$\varepsilon_{\rm cr}(P_2)$	$\varepsilon_{\rm cr}(P_3)$	$\varepsilon_{\rm cr}(P_4)$	$\varepsilon_{\rm cr}(P_5)$	$\varepsilon_{\rm cr}(P_6)$	$\varepsilon_{\rm cr}(P_7)$	$\varepsilon_{\rm cr}(P_8)$
0.12	3×10^{-14}	120×10^{-9}	1.7	6.6	5	4.5	3.5	2.95	2.6	**2.55**
0.24	3×10^{-14}	60×10^{-9}	1.7	2.2	3.4	**1.75**	2.05	2.25	2.2	2.45
0.24	3×10^{-14}	120×10^{-9}	1.7	5.45	4.75	4.3	3.45	2.85	**2.5**	**2.5**
0.24	3×10^{-14}	120×10^{-9}	3.4	13.5	6.35	9.6	5.6	6.95	7.3	**5.95**
0.24	3×10^{-14}	300×10^{-9}	1.7	–	19.5	12.55	10.7	4.1	3.45	**3.15**
0.48	3×10^{-14}	120×10^{-9}	1.7	4.65	4.1	3.85	3.15	3.3	**2.25**	**2.25**
0.24	6×10^{-14}	60×10^{-9}	1.7	**2.3**	3	3.4	2.5	3.6	3.4	3.7
0.24	12×10^{-14}	60×10^{-9}	1.7	**2.5**	2.6	3.3	4.5	5	5.9	6.9

A. Effect of sound properties and initial distance

We consider a typical coated microbubble that is initially spherical with a radius of $R_0 = 3.6\,\mu$m, coated with a shell that is stress free at static equilibrium with area dilatation modulus $\chi = 0.24$ N/m, bending modulus $k_B = 3 \times 10^{-14}$ N m, and shell viscosity $\mu_s = 60 \times 10^{-9}$ kg/s. The protective shell is assumed to obey the Mooney-Rivlin constitutive law with the degree of softness b set to zero [21,27]. The surface tension σ is set to 0.051 N/m, the polytropic ideal gas constant to $\gamma = 1.07$, the surrounding liquid is assumed to have the properties of water, and the far field static pressure is taken to be the standard ambient pressure of 1 atm. Figure 3 presents

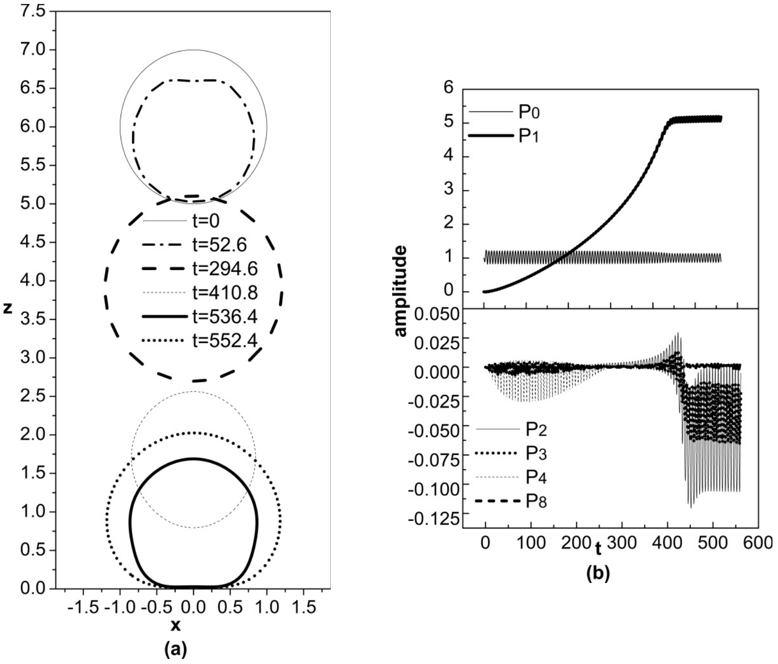

FIG. 3. Temporal evolution of (a) bubble shape and (b) breathing P_0, translational P_1 modes, and shape mode decomposition; the initial bubble radius is $R_0 = 3.6\,\mu$m; shell properties are $\mu_s = 60 \times 10^{-9}$ kg/s, $\chi = 0.24$ N/m, and $k_B = 3 \times 10^{-14}$ N m; the initial distance from the wall is set to $z_{c0} = 6$; an acoustic disturbance of forcing frequency $f = 1.7$ MHz and sound amplitude $\varepsilon = 2$ is imposed.

simulations of the dynamic response of this particular microbubble for an initial distance from the wall of $z_{c0} = 6$ and a sound amplitude of $\varepsilon = 2$. It essentially reproduces Fig. 6 from paper I where the dynamic response of the same microbubble was examined before it reaches the wall. In the latter study it was found that, before the bubble is trapped on the wall, it is accelerated towards it as a result of the secondary Bjerknes forces, mainly during compression. In the same time frame the secondary Bjerknes force F_B is balanced by viscous drag from the surrounding fluid F_D, and the average speed of the center of mass is initially proportional to the inverse of the square of the distance from the wall, as shown in paper I of the present study, with the dependence shifting to the inverse distance from the wall as the latter is approached by the bubble:

$$F_B = 2\pi\rho\delta_o^2\omega_f^2R_0^4\left(\frac{R_0}{2\langle z'_c\rangle}\right)^2 = F_D = \frac{c_D}{2}\rho\langle U'\rangle^2\pi R_0^2 \tag{14}$$

with the drag coefficient, c_D, obeying a law pertaining to a no-slip interface [32,33] for $\mathrm{Re} \gg 1$ when the translational Reynolds $\mathrm{Re}_T \geqslant 1$:

$$c_D = \frac{24}{\mathrm{Re}_T}\left[1 + 0.15\mathrm{Re}_T^{0.687}\right], \quad \mathrm{Re}_T \equiv \frac{\rho U 2R_0}{\mu}. \tag{15}$$

In the above formulas δ_o denotes the maximum dimensionless radius excursion from equilibrium, Re_T is the translational Reynolds number, $\langle z'_c\rangle$ is the dimensional distance from the wall, and $\langle U'\rangle$ is the translational velocity of the bubble center of mass, both averaged over a period of the volume pulsation. Due to the nature of the Bjerknes force $\langle U'\rangle$ exhibits a quadratic variation with time as can be gleaned from Fig. 3 where the time evolution of P_0 and P_1 is shown, Fig. 3(b). Since the forcing frequency ω_f is used as the characteristic time scale, $t/(2\pi)$ provides a rough estimate of the number of periods that have elapsed in terms of the imposed sound field, especially as t increases. Wall proximity instigates bubble deformation that is primarily represented by the gradual growth of P_2 and P_3 as the distance from the wall decreases, due to the Bjerknes bubble/wall interaction. Furthermore, the translating microbubble acquires a prolate shape due to excessive compression at the equator region in response to the viscous drag, which becomes more intense as the distance from the wall decreases, that causes a buildup of the shell viscous stress in the vicinity of the south pole thus relaxing the compressive elastic strain that develops in the latter region in response to the liquid overpressure.

The above response pattern is halted as the bubble reaches the wall in the sense that the translational motion is decelerated while the bubble interface reverts from prolate to oblate, as illustrated by the shapes in Fig. 3(a) and the time evolution of the amplitudes of shape modes shown in Fig. 3(b). The shape of the interface in Fig. 3(a) is illustrated in terms of the axial cylindrical coordinate z and the Cartesian coordinate $x = r_{\mathrm{sph}}\cos\theta$; r_{sph}, θ, φ denote spherical coordinates with φ set to 0 in Fig. 3(a). In the present study we focus on the behavior of the microbubble during the phase of its motion in which the bubble performs trapped pulsations in the immediate vicinity of the wall. Figure 4 illustrates the latter response pattern. In fact, as can be gleaned from the mode decomposition in Fig. 4(a) the radial and translational pulsations of the bubble are in phase, with the microbubble exhibiting minimum distance from the wall, i.e., maximum P_1 amplitude, when it achieves maximum compression, i.e., maximum absolute P_0 amplitude. Furthermore, in this phase of the pulsation a lubrication pressure is established in the region between the bubble south pole and the wall where a maximum overpressure on the part of the liquid gradually develops, Figs. 4(b) and 4(d). It is this lubrication pressure that now balances the Bjerknes force, rather than the viscous drag as was the case during acceleration towards the wall [20], thus resisting further advancement of the microbubble towards the wall. This is also illustrated in Figs. 4(b) and 4(c) and Figs. 4(d) and 4(e) obtained at the time instants pertaining to maximum compression and expansion respectively, during which the liquid overpressure along the axis of symmetry is reversed in favor of the pole region adjacent to the wall rather than away from it, especially in the expansion phase of the pulsation. Eventually, after a few cycles of oscillation an equilibrium is established between

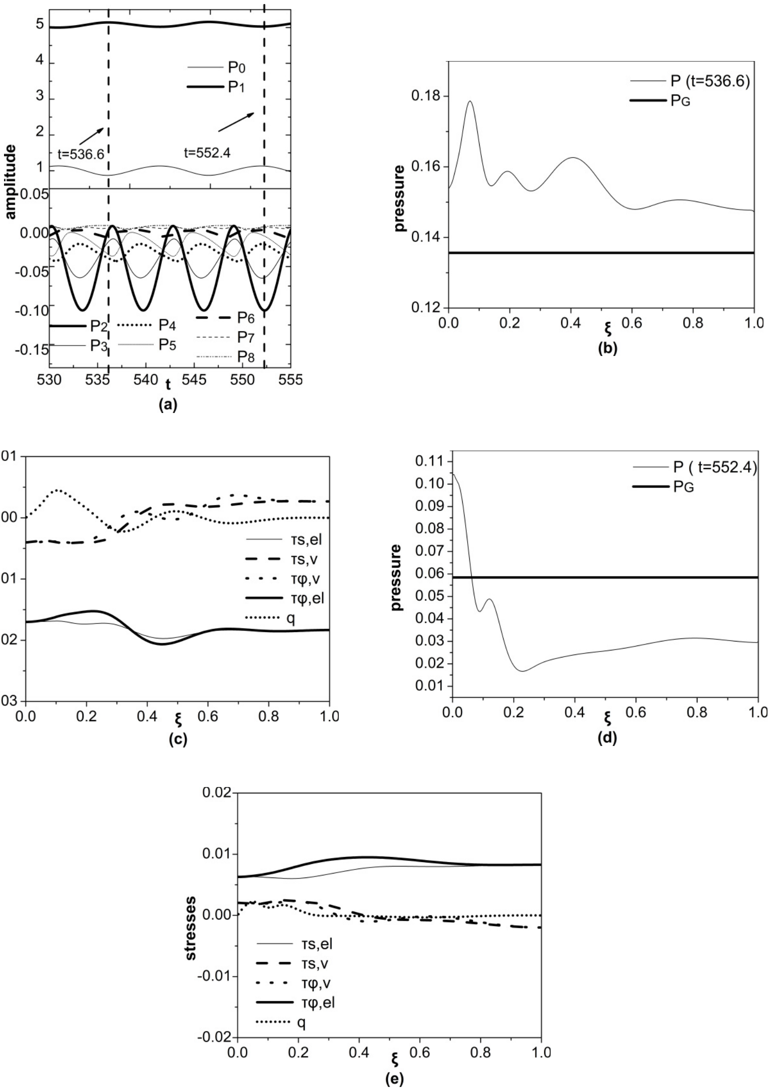

FIG. 4. (a) Zoom-in on the shape mode evolution during trapped oscillations; interfacial distribution of (b), (d) pressure, and (c),(e) viscoelastic stresses, at maximum compression and expansion respectively during trapped pulsations; the initial bubble radius is $R_0 = 3.6\,\mu$m; shell properties are $\mu_s = 60 \times 10^{-9}$ kg/s, $\chi = 0.24\,$N/m and $k_B = 3 \times 10^{-14}$ N m; the initial distance from the wall is set to $z_{c0} = 6$; an acoustic disturbance of frequency $f = 1.7$ MHz and sound amplitude $\varepsilon = 2$ is imposed.

Bjerknes attraction and the lubrication pressure that is generated. At the same time interval the shell interface is flattened in the region near the wall signifying the onset of significant shell compression and bending, in response to the point force exerted on it by the lubrication pressure.

The bubble is thus trapped on the wall where it performs pulsations with an average distance from it that is less than 100 nm. This behavior is evident from Figs. 3(b) and 4(a) where a steady pulsation is registered of modes P_0 and P_1 as well as of the shape modes during this phase of the bubble response. When trapped oscillations of the microbubble take place, growth of shape modes, e.g., P_2, P_3, P_4, P_5, P_6, P_7, occurs in a subharmonic fashion during both the expansion and compression phases of the pulsation, Fig. 4(a), since the bubble remains in the vicinity of the wall and exhibits deformation throughout its pulsation. The maximum overpressure in favor of the surrounding liquid that occurs in the south pole region near the wall, Figs. 4(b) and 4(d), signifies the lubrication effect that arises in the near wall region which, averaged over a period of the pulsation, is responsible for balancing the Bjerknes force and halting the bubble translation while determining the extent of the flattened shell region, as will be seen in more detail in the following. The lubrication pressure is locally balanced by the transverse shear stress resultant q, Figs. 4(c) and 4(e), that arises due to shell bending and leads to a flattened shape; hence a more appropriate terminology for this effect would be elastolubrication. The compressive elastic stresses that develop in the south pole region due to liquid overpressure are attenuated due to the onset of shell viscous stresses, Figs. 4(c) and 4(e). Furthermore, at maximum expansion and away from the wall region the bubble interface exhibits a positive overpressure in favor of the enclosed gas that causes expansion of the shell which acquires maximum elongation near the equator, Figs. 4(d) and 4(e). This is expected during the expansion phase because liquid is forced to leave the two poles and move towards the equator where a local minimum in the liquid pressure is established. As a result the elastic stresses acquire a maximum in the equator region, in order to balance the overpressure in the interior of the bubble, where elongation takes place, Fig. 4(e), hence the oblate shapes registered in the simulation, Fig. 3(a), and the negative sign of the amplitude of P_2, Fig. 4(a), during trapped pulsations. Overall, during trapped pulsations and at maximum expansion and compression, bending and elastic stresses form the dominant balance with overpressure in the wall vicinity and far from the wall, respectively, and this determines the degree of shell deformation.

Next, the above simulation is repeated for a smaller initial distance from the wall and the same properties of the acoustic excitation, i.e., $\varepsilon = 2$, $\omega_f = 2\pi 1.7\,\mathrm{MHz}$, and $z_{c0} = 4$. Figures 5(a) and 5(b) depict the results of the simulations in terms of the evolution of the bubble shape and its mode decomposition. The microbubble exhibits the same pattern of initial acceleration due to the secondary Bjerknes forces until it reaches the rigid boundary in which case it performs trapped pulsations with the lubrication pressure balancing Bjerknes forces. Once the bubble reaches the vicinity of the wall the onset of oblate shapes is captured that are dominated by P_2 and P_3, mainly in the expansion phase of the pulsation during which the lubrication effect is maximized, as opposed to prolate shapes that prevailed at larger distances from the wall, mostly in the compression phase during which bubble deformation is more intense. Growth of higher shape modes takes place in the phase of trapped pulsations in this case as well, albeit in a subharmonic manner as opposed to harmonic resonance that was the case far from the wall, Fig. 10 in paper I, due to the decrease of the breathing mode frequency with decreasing wall distance. The same distinction in the dynamic pattern is exhibited in the case with $z_{c0} = 6$, Fig. 7 in paper I vs Fig. 4 in the present paper. Nevertheless, parametric shape mode excitation always remains subdominant to growth of P_2 and P_3 due to wall interaction; see also the zoom in on the growth of shape modes during trapping provided in Fig. 5(c). The shape of the bubble during trapping, Fig. 5(a), is hardly distinguished from the one obtained for a larger initial distance from the wall, Fig. 3(a), signifying the same order of magnitude of the secondary Bjerknes force and the resulting deformation at trapping. Consequently, the bubble speed and force at the onset of trapping do not depend significantly on the initial distance, for fixed shell and sound properties, and it will be sufficient to evaluate them by starting the simulation with the bubble initially located at a relatively small dimensionless distance, e.g., $z_{c0} \approx 2$, in order to minimize the time required to simulate the entire process. It should also be stressed that in both cases, $z_{c0} = 6$ and $z_{c0} = 4$, the bubble is finally trapped on roughly the same distance from the wall, $z_c \approx 0.75$, and exhibits the same order of magnitude of flatness in the near wall region. This is also manifested in the evolution and magnitude of the shape modes, Figs. 5(b) and 5(c), that exhibit the same pattern as in Figs. 3(b) and 4(a) despite the fact that the bubble reaches the wall, i.e., within less than one bubble radius from the wall, within a different time frame that is on the order ${z_{c0}}^2$. This signifies the inverse distance dependence of the center of mass average speed as the microbubble approaches the wall predicted by the balance between secondary Bjerknes force and viscous drag provided in Eqs. (14) and (15) during the phase of accelerating motion of the microbubble towards

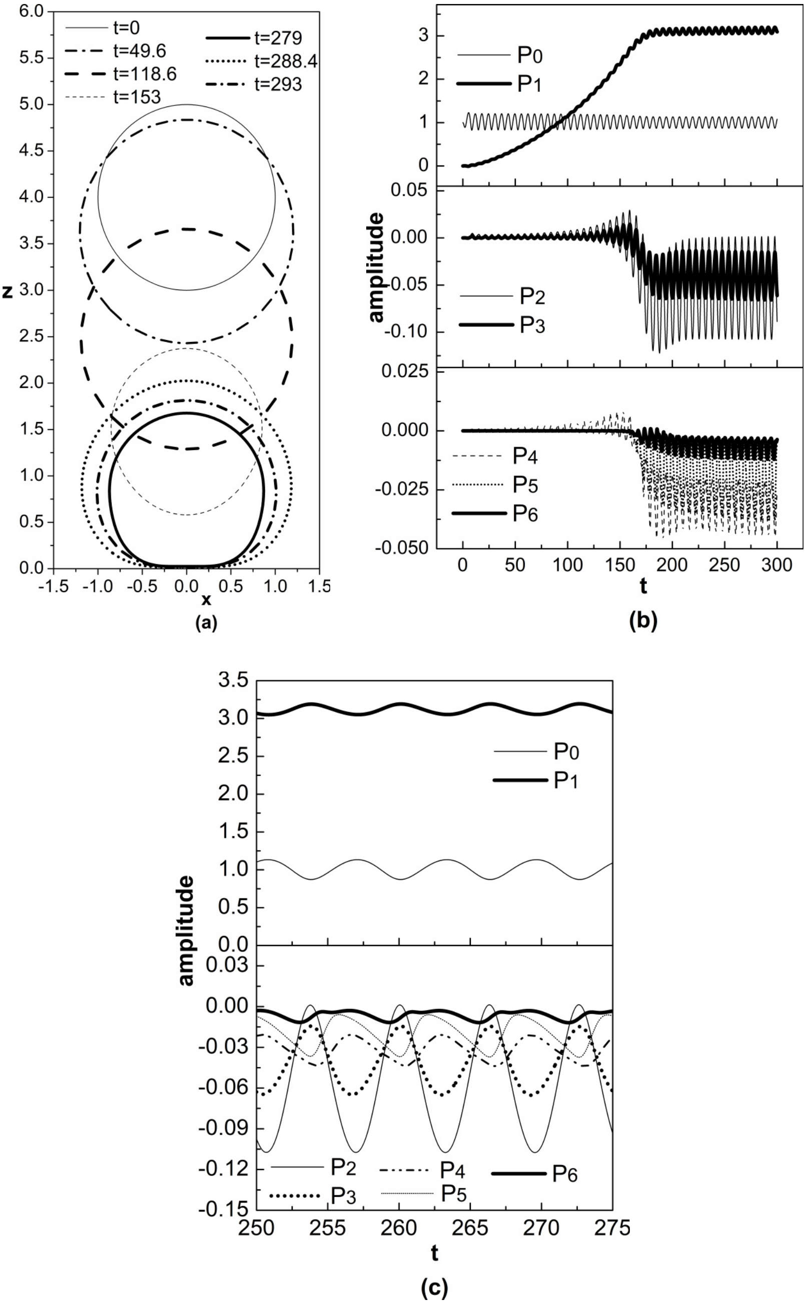

FIG. 5. Temporal evolution of (a) bubble shape, (b) breathing P_0, translational P_1 modes, and shape mode decomposition, and (c) zoom-in on the shape mode evolution during trapped oscillations; the initial bubble radius is $R_0 = 3.6\,\mu$m; shell properties are $\mu_s = 60 \times 10^{-9}\,$kg/s, $\chi = 0.24\,$N/m and $k_B = 3 \times 10^{-14}\,$N m; the initial distance from the wall is set to $z_{c0} = 4$; an acoustic disturbance of frequency $f = 1.7$ MHz and sound amplitude $\varepsilon = 2$ is imposed.

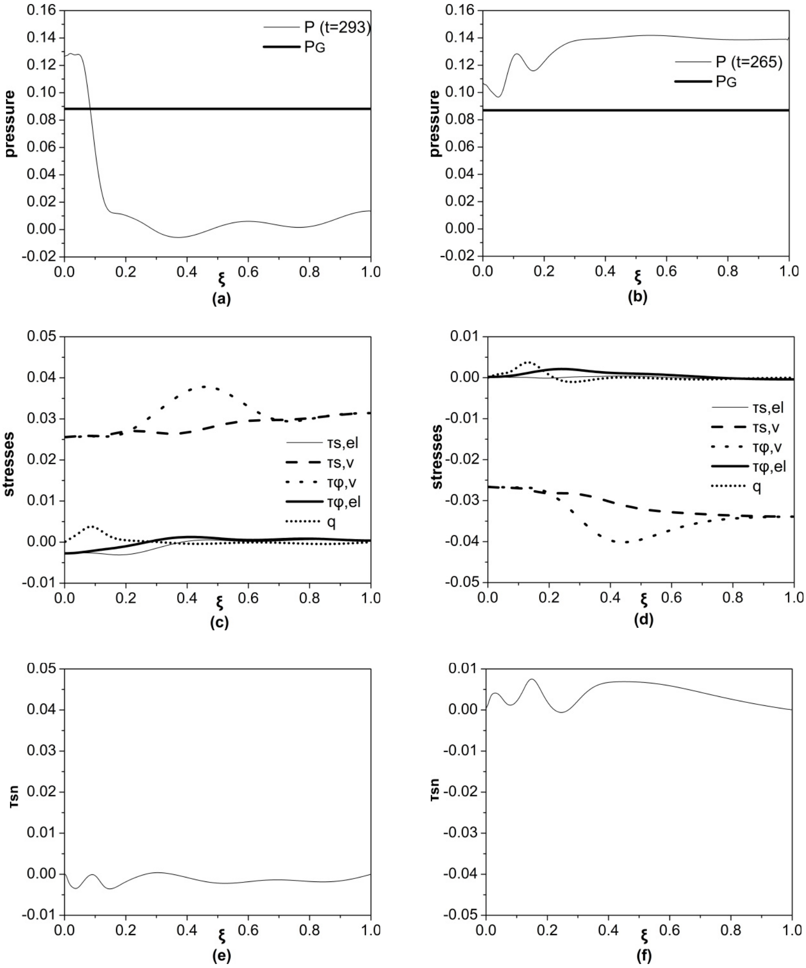

FIG. 6. Interfacial distribution of (a),(b) pressure, (c),(d) shell viscoelastic stresses, and (e),(f) liquid viscous tangential stresses when the volume pulsation crosses from compression to expansion and vice versa, respectively, during trapped pulsations; the initial bubble radius is $R_0 = 3.6\,\mu\text{m}$; shell properties $\mu_s = 60 \times 10^{-9}\,\text{kg/s}$, $\chi = 0.24\,\text{N/m}$ and $k_B = 3 \times 10^{-14}\,\text{N m}$; the initial distance from the wall is set to $z_{c0} = 4$; an acoustic disturbance of frequency $f = 1.7$ MHz and sound amplitude $\varepsilon = 2$ is imposed.

the wall. Based on the latter balance we can write $\langle U\rangle \sim \frac{\Delta\langle z_c\rangle}{\Delta t} \sim \frac{1}{\Delta\langle z_c\rangle} \rightarrow \Delta t \sim \Delta\langle z_c\rangle^2 \sim z_{c0}^2$ for a large enough initial distance; see also Fig. 8 in paper I that is obtained for a relatively large initial distance from the wall, $z_{c0} = 6$.

The stress distribution along the shell at maximum compression and expansion during trapped pulsations is also in agreement with the prediction obtained for a larger initial distance in Figs. 4(b)–4(e), with shell bending and elastic strain forming the dominant balance with liquid lubrication pressure in the south pole region and gas-liquid overpressure in the bulk of the shell, respectively. Overall, the lubrication pressure resists Bjerknes attraction during this phase of the bubble pulsation. In addition, Figs. 6(a)–6(d) illustrate the distribution of internal and liquid pressure at the interface as well as of the elastic stresses at the time instants for which the volume pulsation crosses from compression to expansion and vice versa, respectively; corresponding shapes are provided in Fig. 5(a). It should be stressed that Fig. 5(a) only contains a snapshot corresponding to the passing from compression to expansion ($t = 293$), as the shape of the interface is almost

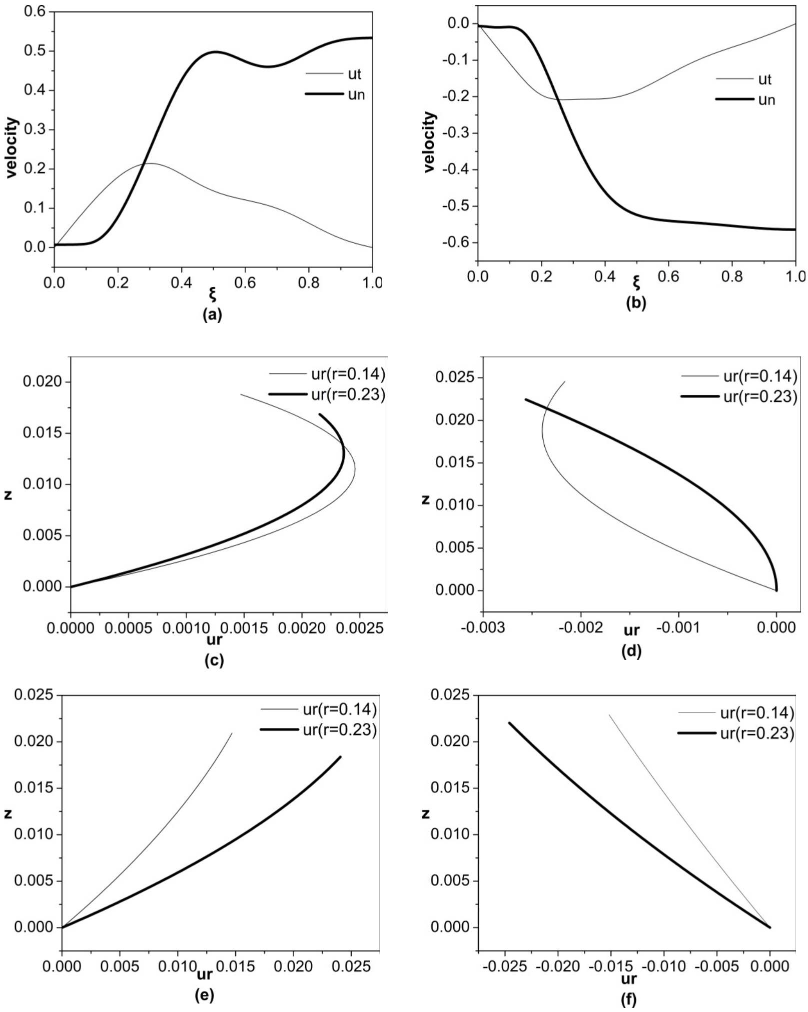

FIG. 7. (a),(b) Interfacial distribution of tangential and normal velocities when the volume pulsation crosses from compression to expansion and vice versa, respectively, (c)–(f) velocity profile during maximum expansion, maximum compression, and when the volume pulsation crosses from compression to expansion and vice versa, respectively, during trapped pulsations; the initial bubble radius is $R_0 = 3.6\,\mu$m; shell properties are $\mu_s = 60 \times 10^{-9}$ kg/s, $\chi = 0.24$ N/m and $k_B = 3 \times 10^{-14}$ N m; the initial distance from the wall is set to $z_{c0} = 4$; an acoustic disturbance of frequency $f = 1.7$ MHz and sound amplitude $\varepsilon = 2$ is imposed.

identical when the opposite motion takes place. In these two time instants pertaining to Figs. 6(a) and 6(c) [Figs. 6(b) and 6(d)], the breathing mode pulsation acquires maximum positive (negative speed). This can also be gleaned by the distribution of the tangential and normal velocity along the shell-liquid interface shown in Figs. 7(a) and 7(b). Both velocity components are positive (negative) in Fig. 7(a) [Fig. 7(b)], signifying the tendency of the bubble to expand (contract) and translate away from (towards) the wall and this can be verified by simple inspection of the mode decomposition in the zoom-in provided in Fig. 5(c) that exhibits the same pattern. As can be gleaned from these plots, the shape of the bubble remains mostly spherical away from the wall, where viscous shell stresses along with surface tension and gas or liquid overpressure dominate the normal force balance of shell equilibrium. Elongational (compressive) viscous shell stresses develop, Fig. 6(c) [Fig. 6(d)], in order to balance the positive (negative) overpressure of the bubble interior, Fig. 6(a) [Fig. 6(b)],

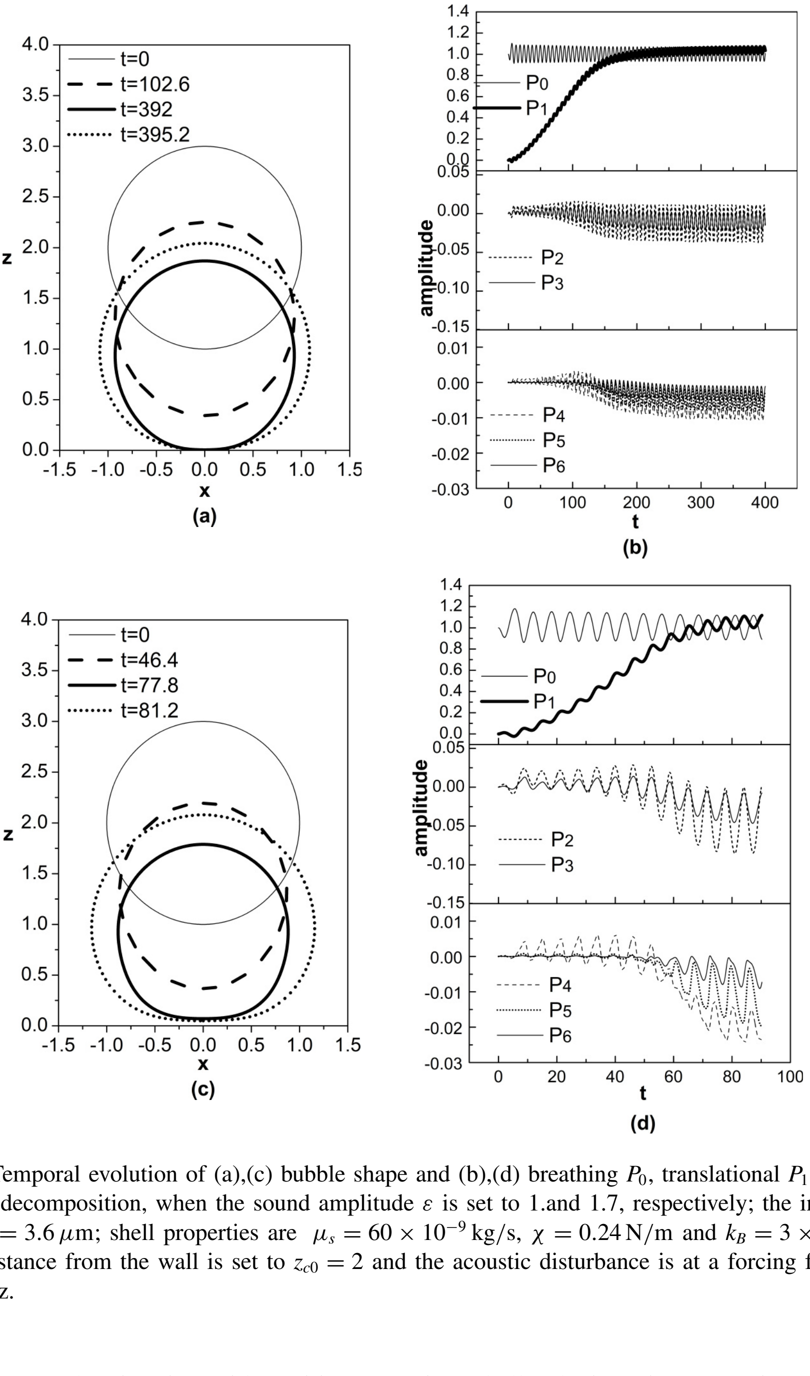

FIG. 8. Temporal evolution of (a),(c) bubble shape and (b),(d) breathing P_0, translational P_1 modes, and shape mode decomposition, when the sound amplitude ε is set to 1.and 1.7, respectively; the initial bubble radius is $R_0 = 3.6\,\mu\text{m}$; shell properties are $\mu_s = 60 \times 10^{-9}$ kg/s, $\chi = 0.24$ N/m and $k_B = 3 \times 10^{-14}$ N m; the initial distance from the wall is set to $z_{c0} = 2$ and the acoustic disturbance is at a forcing frequency of $f = 1.7$ MHz.

corresponding to the situation with positive (negative) shell velocity, Fig. 7(a) [Fig. 7(b)]. In the vicinity of the wall, bending stresses develop in conformity with the pressure distribution in order to counteract Bjerknes attraction to the wall. The purely elastic strain remains subdominant in these time instants with bending and viscous shell stresses forming the dominant balance with overpressure, near the south pole facing the wall and the bulk of the shell, respectively, based on the normal force balance. On the other hand, according to the tangential force balance viscous stresses develop in the liquid that surrounds the shell and follow variations of shell viscous stresses

TABLE II. Translational velocity at a distance 1.2 from the wall for different sound amplitudes; shell parameters are $\mu_s = 60 \times 10^{-9}\,\mathrm{kg/s}$, $\chi = 0.24\,\mathrm{N/m}$, $k_B = 3 \times 10^{-14}$ N m; the acoustic disturbance is at a forcing frequency of $f = 1.7$ MHz.

ε	δ_0	U
1	0.087	0.0054
1.7	0.147	0.0159
2	0.205	0.0196

in the bulk of the shell and as the contact region is approached, whereas they follow variations in the transverse shear q in the contact region. Figure 6(e) [6(f)] provides indicative profiles of liquid shear stress along the shell interface, illustrating a shear force that pushes (pulls) liquid out of (into) the gap; in order to compare against the shell viscous stresses the shear due to liquid viscosity is multiplied by $1/\mathrm{Re}$. The gap region is formed in the region below the flattened part of the interface when the microbubble performs trapped pulsations.

An important aspect of the bubble pulsation during trapping is the state of motion in the fluid which is characterized by a weak pressure driven flow, Figs. 7(c) and 7(d) during maximum compression and expansion while developing an oscillatory Stokes shear layer with zero mean velocity in the wall vicinity, Figs. 7(e) and 7(f), when the shell velocity becomes maximum, positive, or negative; see also Figs. 7(a) and 7(b). The distribution of tangential and normal velocity along the shell-liquid interface for the time instants pertaining to maximum expansion or compression is not provided as it is much weaker and results in a weak Poiseuille type flow arrangement, Figs. 7(c) and 7(d). The situation with maximum positive or negative shell velocity is provided in Figs. 7(a) and 7(b), which illustrate a region of zero normal velocity near the axis of symmetry in the region next to the wall. It is the same region where shell flattening takes place and the oscillatory pressure driven and shear flow patterns appear, Figs. 7(c)–7(f), with an alternating direction that is dictated by the frequency of the volume pulsation. The oscillatory part of the motion averages out to zero over the forcing period and there is no indication of a streaming motion or the appearance of any kind of vortex formation. The same is true for the fluid region away from the wall that exhibits the same kind of oscillatory behavior following the volume pulsation with the fluid moving away from or towards the contact region with the wall during transition from compression to expansion and expansion to compression, respectively.

In order to assess the effect of sound amplitude on the process of microbubble acoustic trapping in the vicinity of the rigid wall we repeat the above simulation for smaller sound amplitudes, i.e., $\varepsilon = 1.7$ and 1, and a shorter initial distance $z_{c0} = 2$ to minimize computational cost. The dynamic response pattern that is obtained in this fashion is illustrated in Fig. 8 indicating a similar trend as in Figs. 3 and 5, especially regarding the time evolution of the shape mode decomposition which is dominated by P_2 and P_3 in the manner previously described. The shape that is acquired by the microbubble while performing trapped pulsations varies with the sound amplitude, in the sense that it becomes progressively more flattened in the region around the south pole as the sound amplitude increases; see also the last two shapes in Figs. 3(a), 8(a), and 8(c) corresponding to the time instants of maximum expansion and compression, respectively. Furthermore, the average speed of the bubble center of mass tends to increase for increasing sound amplitude. More specifically, the Bjerknes force depends quadratically on the sound amplitude; see also Eq. (14). In addition, and as Re_T increases, the viscous drag force may vary linearly or quadratically with the translational velocity, see also Eq. (15), which in its turn increases quadratically or linearly with respect to the sound amplitude ε, or δ_o in terms of the radial pulsation, in order to maintain the balance with Bjerknes force. This is corroborated by numerical evaluation of the translational speed slightly before trapping is achieved, as shown in Table II where the translational velocity that corresponds to the simulations of Figs. 5(b), 8(b), and 8(d) is reported. For small ε values the average translational

TABLE III. Dimensionless time t_1 required for the bubble to reach the wall as a function of sound amplitude; shell parameters for the case of acoustic frequency 1.7 MHz are $\mu_s = 60 \times 10^{-9}\,\mathrm{kg/s}$, $\chi = 0.24\,\mathrm{N/m}$, $k_B = 3 \times 10^{-14}\,\mathrm{N\,m}$, and for the case of 3.4 MHz $\chi = 0.24\,\mathrm{N/m}$, $\mu_s = 120 \times 10^{-9}\,\mathrm{kg/s}$, and $k_B = 3 \times 10^{-14}\,\mathrm{N\,m}$; the initial bubble radius is $R_0 = 3.6\,\mu\mathrm{m}$ and the initial distance from the wall is set to $z_{c0} = 2$.

$f = 1.7\,\mathrm{MHz}$			$f = 3.4\,\mathrm{MHz}$		
ε	δ_0	t_1	ε	δ_0	t_1
1	0.087	172	3	0.045	259.6
1.7	0.147	64.75	4	0.06	152.7

velocity is relatively small and this favors a nearly quadratic dependence with ε or δ_0, whereas as the sound amplitude increases Re_T increases as well and a quadratic dependence of drag force with respect to the translational velocity emerges which reflects in an almost linear dependence of $\langle U \rangle$ with ε or δ_0. A similar result was obtained in paper I regarding the dependence of translational velocity $\langle U \rangle$ on the average distance from the wall $\langle z_c \rangle$, where an inverse distance dependence was registered for ε set to 2; see also Fig. 8 of paper I.

It should also be stressed that the wall suppresses parametric mode excitation and allows for trapped oscillations adjacent to the wall up to a threshold amplitude $\varepsilon \approx 2$, which is slightly larger than the threshold $\varepsilon \approx 1.7$ for parametric mode excitation obtained by stability analysis for a freely pulsating contrast agent ignoring viscous effects in the surrounding liquid.

An important relevant issue is raised as to what can be done in order to facilitate the trapping procedure for greater disturbances. In an effort to investigate this possibility we repeat the above simulations, but for twice as large an external frequency which is now set to 3.4 MHz and a larger shell viscosity $\mu_s = 120 \times 10^{-9}\,\mathrm{kg/s}$. Figure 9 presents the response pattern captured by the simulations for this case with increased sound amplitude ε that is set to 3 and 4. Linear stability analysis predicts an amplitude threshold for parametric mode excitation on the order of 4, see also Table I, for this parameter range and this trend is corroborated by the simulations shown in Fig. 9, where trapping of the bubble is now captured for a disturbance with an amplitude as large as $\varepsilon = 4$. In fact, by increasing the external frequency and shell viscosity the volume and shape pulsations become less intense due to the increased combined effect of shell viscosity. As a result, the secondary Bjerknes force is decreased and translation of the center of mass takes place at a lower speed as predicted by the dominant force balance in Eq. (14). Thus, Re_T is relatively small and the drag force depends linearly on the average bubble translational velocity which in its turn depends quadratically on the sound amplitude, i.e., $U \equiv \langle \dot{z}_c \rangle \sim \delta_o^2$ with δ_o denoting the amplitude of radial motion. Consequently the dimensionless time required to reach the wall, for fixed forcing frequency and initial distance from the wall, is inversely proportional to δ_o^2 as can be gleaned by examining the time evolution of P_1 in Figs. 8(b) and 8(d) and Figs. 9(b) and 9(d); see also Table III where t_1 denotes the time needed for the bubble center of mass to become $\langle z_c \rangle \approx 1$.

In both Figs. 8 and 9 the pattern of trapped pulsation characterized by in phase volume and center of mass pulsations is recovered. Furthermore, the motion is purely oscillatory without an acoustic streaming component, as expected due to the in phase radial and lateral pulsation of the microbubble [13]. Throughout the present study no parameter range was identified for which a significant phase lag was observed. This response pattern is partly due to the shell material that can sustain a significant amount of shear, as opposed to a conventional bubble that obeys a zero shear interfacial condition, but also due to the manner in which the translation of the center of mass is triggered by the wall presence, and finally due to the fact that the sound amplitude was not raised high enough to generate significant inertia effects that might detune the volume and center of mass pulsations. The sound amplitude was maintained at a relatively small level in order

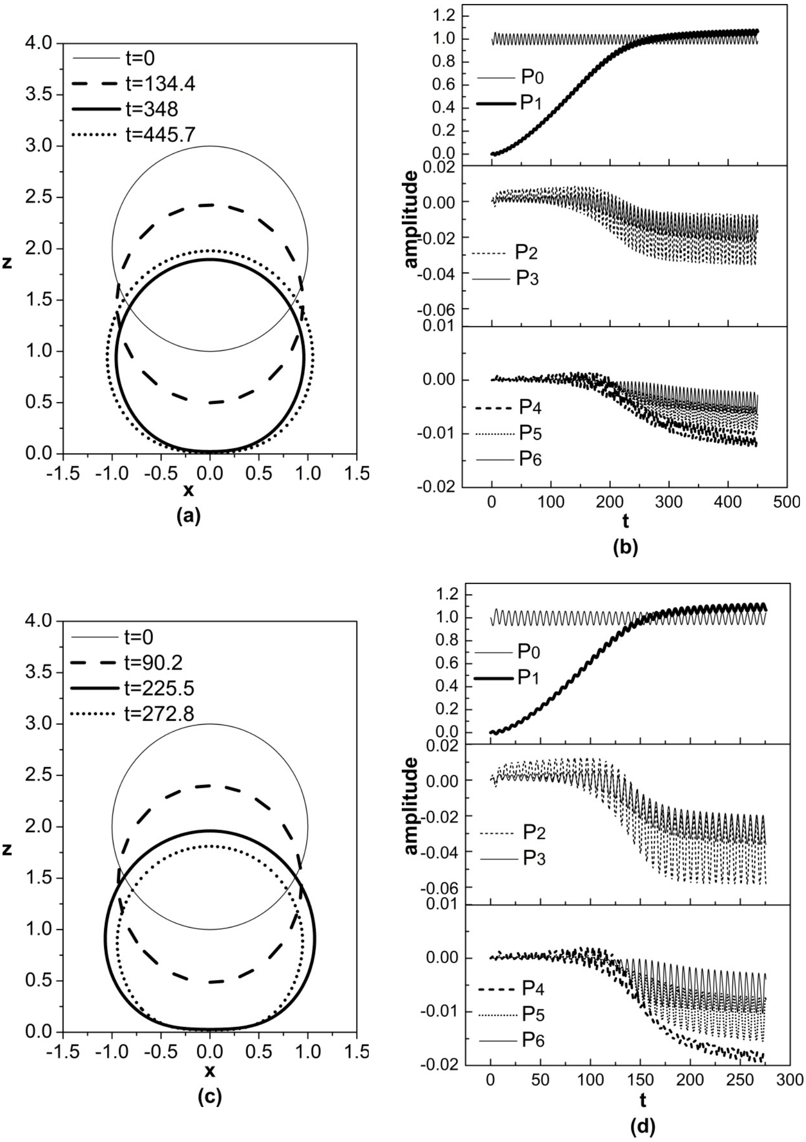

FIG. 9. Temporal evolution of (a),(c) bubble shape and (b),(d) breathing P_0, translational P_1 modes, and shape mode decomposition, when the sound amplitude ε is set to 3 and 4, respectively; the initial bubble radius is $R_0 = 3.6\,\mu\mathrm{m}$; shell properties are $\chi = 0.24\,\mathrm{N/m}$, $\mu_s = 120 \times 10^{-9}\,\mathrm{kg/s}$, and $k_B = 3 \times 10^{-14}\,\mathrm{N\,m}$; the initial distance from the wall is set to $z_{c0} = 2$ and the acoustic disturbance is at a forcing frequency of $f = 3.4$ MHz.

to exclude the possibility for parametric shape mode excitation that would lead to bubble breakup and compromise the accuracy of the simulations. Therefore, we operate at a small steady streaming Reynolds, $\mathrm{Re}_{\mathrm{st}} = \delta_o^2 \mathrm{Re}^{1/2} \ll 1$ in which case the analysis in [13] is valid and, in the absence of a significant phase difference, no steady streaming component was captured in the flow domain.

B. Time average force balance and the effect of shell properties

The evolution of the time average force balance over a period of the pulsation is also of interest in order to assess the mechanism that determines the shell configuration leading to the

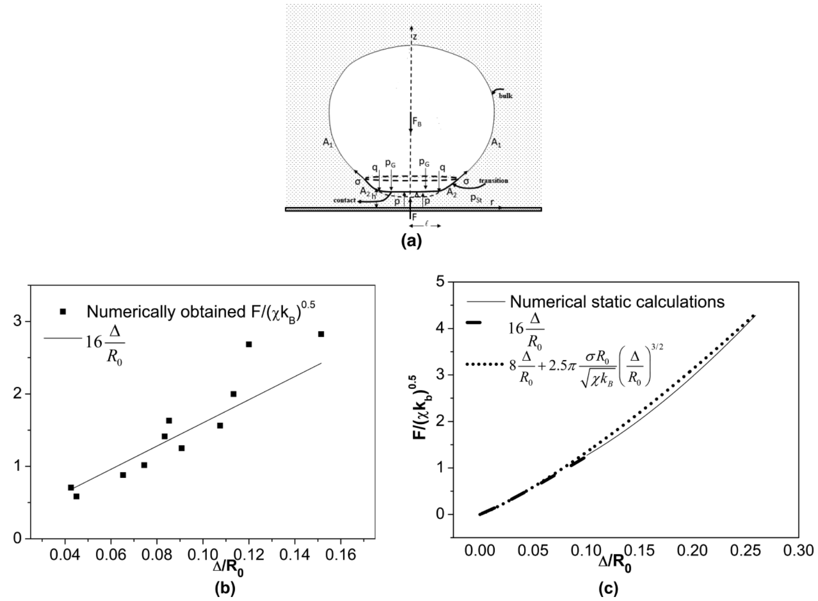

FIG. 10. (a) Schematic diagram of the time averaged force balance in the near wall region of the microbubble, (b) values obtained for $\frac{F_B}{\sqrt{\chi k_B}}$ numerically and comparison with the function $16\Delta/R_0$, and (c) numerical obtained static calculations and fitting of the results [31].

onset of steady pulsations. Since a steady pulsation is indeed eventually achieved the force that counteracts the secondary Bjerknes force has to be identified. In the nearly flat part of the shell (contact region) that lies in the vicinity of the wall the dominant balance is between the lubrication pressure and the variation of transverse shear stress resultant, $\partial q/\partial s$, that arises as the shell bends in order to withstand the lubrication pressure that develops in the surrounding liquid in order to counteract the secondary Bjerknes force that pushes the bubble towards the wall.

As was seen in the previous subsection, during maximum expansion in the shell region away from the wall a combination of capillary pressure and elastic strain balance gas overpressure across the shell giving rise to an oblate shape, while bending and viscoelastic strain balance lubrication pressure in the contact region. On the other hand, during the phase of maximum interfacial speed, corresponding to the volume pulsation crossing from expansion to compression and vice versa, away from the contact region it is viscous elastic stress that balances overpressure relegating elastic strain and bending stresses to a subdominant effect. The flow arrangement in that region is oscillatory and does not contribute to the time-averaged force balance. Tangential viscous stresses from the surrounding liquid acquire a local maximum, Figs. 6(e) and 6(f), as they have to balance viscous elastic stresses generated on the shell, Figs. 6(c) and 6(d), according to the tangential force balance. This balance holds until the transition region that joins the bulk of the shell with the contact region, Fig. 10(a). In fact, it is the extent of viscous tangential shear from the surrounding liquid that is required to balance viscous elastic stresses that determines the film thickness in the contact region, as will be seen in the next subsection, Sec. IV C. In the contact region lubrication pressure and bending and elastic strain dominate the normal force balance. In particular, it is the extent of bending that is required to balance lubrication pressure that determines the average contact length during a period of the forcing, whereas variations in the bending strain q determine viscous shear in the liquid occupying the gap between the shell and the wall.

Consequently, the flow around the bulk of the shell is nearly ideal with viscous stresses in the liquid passively following the viscous stresses on the shell whereas in the gap region liquid shear generates a Stokes layer type flow parallel to the wall. Therefore, the total force acting on the microbubble in the direction of the axis of symmetry is provided by the integral of the pressure on its interface:

$$\begin{aligned}
F_T\boldsymbol{e}_z &= \iint_{A_1} P\boldsymbol{e}_z\cdot\boldsymbol{n}dA_1 + \iint_{A_2} P\boldsymbol{e}_z\cdot\boldsymbol{n}dA_2\\
&= \iint_{A_1} P\boldsymbol{e}_z\cdot\boldsymbol{n}dA_1 + \iint_{A_2} P\boldsymbol{e}_z\cdot\boldsymbol{n}dA_2 + \iint_{A_2} P_{Id}\boldsymbol{e}_z\cdot\boldsymbol{n}dA_2 - \iint_{A_2} P_{Id}\boldsymbol{e}_z\cdot\boldsymbol{n}dA_2\\
\rightarrow F_T\boldsymbol{e}_z &= \iint_{A_1} P\boldsymbol{e}_z\cdot\boldsymbol{n}dA_1 + \iint_{A_2} P_{Id}\boldsymbol{e}_z\cdot\boldsymbol{n}dA_2 + \iint_{A_2} (P-P_{Id})\boldsymbol{e}_z\cdot\boldsymbol{n}dA_2\\
&= F_B(t)\boldsymbol{e}_z + \iint_{A_2} (P-P_{Id})\boldsymbol{e}_z\cdot\boldsymbol{n}dA_2, \qquad (16a)\\
P_{Id} &= P_{\mathrm{st}} + P_{Ac}(r,z;t), \qquad (16b)
\end{aligned}$$

with F_T denoting the total force and A_1, A_2 the bulk of the shell and the contact region, respectively; see also Fig. 10(a). In Eq. (16a) the integral of the pressure around the microbubble interface obtained for ideal flow conditions is taken to provide the Bjerknes force, see also the analysis in Sec. II B in paper I, while the ideal pressure P_{Id} in the gap region between the shell and wall is decomposed into the static P_{st} and acoustic pressure P_{Ac} components. Upon averaging Eq. (16a) over a period of the pulsation during the phase of trapped pulsations the total force averages to zero as well as the average of the acoustic component of the pressure in the gap region where an oscillatory flow pattern is established. Therefore, the Bjerknes force is balanced by the integral of the liquid overpressure with respect to the static pressure along the contact region of the shell, i.e., the lubrication pressure:

$$-\langle F_B(t)\rangle\boldsymbol{e}_z = -F_B\boldsymbol{e}_z \approx \left\langle \iint_{A_2} (P-P_{\mathrm{st}})\boldsymbol{e}_z\cdot\boldsymbol{n}dA_2 \right\rangle = -\langle F_L(t)\rangle\boldsymbol{e}_z \rightarrow F_B = F_L \qquad (16c)$$

$F_L$denotes the lubrication force averaged over a period of the forcing. As was discussed in the previous section, abrupt changes occur in the shell curvature due to wall proximity and lubrication pressure is determined by variations in transverse shear q; see also the normal force balance in Eqs. (4) and (5). Assuming that bending takes place within the narrow contact region where the radial and axial length scales are such that the shell curvature matches that in the bulk of the shell, the dominant normal force balance in that region reads in dimensionless form

$$P - P_G \sim \frac{1}{r}\frac{\partial(rq)}{\partial S} \sim \frac{k_B}{\rho\omega_f^2 R_0^5}\frac{\partial^4 h}{\partial r^4}, \quad z = h(r;t) \qquad (17)$$

with h denoting the thickness of the layer between the wall and the bubble. As a result, the time average force balance reflects the shell equilibrium and flow arrangement in the gap region at the time instants for which the volume pulsation crosses from expansion to compression and vice versa; see also Figs. 6 and 7. This is a similar situation to the case of static interrogation of a spherical elastic shell that is being squeezed by a rigid plate [31]. When the bubble reaches the wall the shell bends and forms a nearly flat contact region in order to develop the shear stress resultant q that is necessary to counteract the lubrication pressure that halts the motion of the center of mass. The total force that results in this fashion is the integral of the lubrication pressure that develops in the contact region which is counteracted by variations in the transverse shear q (elastolubrication pressure), the internal gas pressure, and the surface tension from the bulk of the shell. Upon introducing Eq. (17)

in Eq. (16c) and integrating we obtain

$$F_L = 2\pi \int_S P r dS - 2\pi \ell \frac{1}{\text{We}} \sin\theta \sim 2\pi \int_S \left(\frac{1}{r} \frac{\partial (rq)}{\partial S} + P_G - P_{\text{st}} \right) r dS - 2\pi \ell \frac{1}{\text{We}} \sin\theta$$
$$\approx 2\pi \ell q + (P_G - P_{\text{st}}) \pi \ell^2 - 2\pi \ell \frac{1}{\text{We}} \sin\theta \tag{18}$$

with S, ℓ, θ, denoting the arc length, the length, and angle that matches the contact region with the bulk of the shell, respectively; see also the schematic in Fig. 10(a). For not very large values of the exerted force and for shells whose elastic properties are such that parameter $k_B/(\chi {R_0}^2)$ is not very small, buckling does not take place and the static shell reaction is mainly exerted at the edge of the flat contact region, as demonstrated by Reissner [34] for a shallow shell. The second term in the integrand of Eq. (18) represents the contribution to the force from the region underneath the contact area while the third term represents the contribution from the bulk of the shell onto the contact region due to its surface tension. In this context, upon balancing bending and stretching in the part of the shell that is in "contact" with the wall, the transverse shear q is calculated at the edge of the contact region and the shell deformation Δ is seen to vary almost linearly with the applied force. To illustrate this force balance we plot in Fig. 10(b) the secondary Bjerknes force evaluated via Eq. (14) setting the distance from the wall to twice the bubble radius, i.e., $z_c = 2$, for all the cases discussed in this section for which trapped pulsations were obtained, against the numerically calculated dimensionless deformation Δ of the south pole of the shell averaged over a period of the forcing. Δ is defined as the difference in the distance of the south pole location from the center of mass, measured at stress free conditions and during trapped pulsations in the manner typically employed in shell compression experiments. As can be gleaned from Fig. 10(b) the cloud of points collapses in the line that is closely fitted by Eq. (19a) below:

$$\frac{F_B}{\sqrt{\chi k_B}} \approx 16 \frac{\Delta}{R_0}, \tag{19a}$$

$$\frac{F_B}{\sqrt{\chi k_B}} \approx 8 \frac{\Delta}{R_0} + 2.5\pi \frac{\sigma R_0}{\sqrt{\chi k_B}} \left(\frac{\Delta}{R_0} \right)^{3/2}, \tag{19b}$$

$$P_G - P'_{\text{st}} \approx \frac{2\sigma}{R_0}. \tag{19c}$$

The factor 16 is different from the factor 8 obtained by Reissner because in our case there is an additional stiffness of the shell, apart from the area dilatation and bending moduli χ, k_B, due to surface tension $\sigma = 0.051\,\text{N/m}$ that represents the resistance of the shell against volume compression. In fact, upon calculating the static response of a microbubble with the size and elastic properties of the ones examined in the present study, squeezed between two rigid planes, we obtain the same result in the force deformation curve [31], as illustrated in Fig. 10(c). In particular, in the range of small deformations a nearly linear response is recovered with the slope modified due to surface tension, Eq. (19a). For larger deformations a slightly nonlinear static response pattern is recovered, $O(\Delta/R_0)^{1.5}$, in the manner described by Eq. (19b). The 3/2 type dependence results by adding to the Reissner response that of a conventional bubble that is statically interrogated in the same fashion [31]. It represents the force required to overcome the resistance to compression due to interfacial tension, as the oblateness of the deformed microbubble increases.

Furthermore, the extent of the contact region ℓ scales like $\ell/R_0 = (\Delta/R_0)^{1/2}$ so that the transition region, where bending and membrane stresses balance each other, forms an $O(1)$ curvature to match the bulk of the shell that remains nearly spherical. Upon introducing the Bjerknes force from Eq. (14) in the above linear force deformation law and grouping terms so that dimensionless variables appear we obtain

$$\left(\frac{\ell}{R_0}\right)^2 \approx \frac{\Delta}{R_0} = \frac{2\pi\delta_o^2}{C}\left(\frac{1}{4}\right)^2\sqrt{\frac{\rho\omega_f^2R_0^5}{k_B}}\sqrt{\frac{\rho\omega_f^2R_0^3}{\chi}}, \tag{20}$$

with coefficient C depending on the relative importance of the different shell stiffnesses, $\sigma^2R_0^2/(\chi k_B)$, and the extent of deformation. In particular, when $\Delta/R_0 \sim 0.1$, $\sigma = 0.051\,\mathrm{N/m}$, $k_B = 3 \times 10^{-14}\,\mathrm{N\,m}$ and χ varies between 0.12, 0.24, and 0.48 N/m, then $C(\sigma^2R_0^2/(\chi k_B))$ varies between 19, 16, and 14. Hence the cloud of points obtained by the simulations illustrated in Fig. 10, pertaining to the average deformation during trapped pulsations, conform well with the linear dependence described by Eq. (19a). The progressive increase in the contact length with increasing sound amplitude can also be gleaned by simple inspection of the bubble shape during the phase of trapped pulsations as illustrated in Figs. 5(a), 8(a), and 8(c).

Based on the above analysis we next consider shells with different area dilatation modulus in order to determine how shell elasticity directly contributes to the trapping procedure. In this case also parametric stability controls the dynamic response in terms of the amplitude threshold for steady trapped pulsations to be achieved. As can be gleaned from Table I the phase diagram pertaining to parametric mode excitation is not significantly affected by varying the area dilatation modulus, with the exception of the case with area dilatation χ set to 0.48 N/m for which case the amplitude range for trapped pulsations is reduced, in agreement with stability analysis. Furthermore, as was stressed in the previous subsection, the ratio between stretching and bending resistance, $k_B/(\chi R_0^2)$, is such that buckling does not take place. Hence, gradually increasing the area dilatation from $\chi = 0.12\,\mathrm{N/m}$ to 0.24 and 0.48 N/m while maintaining the rest of the shell parameters, as well as the forcing frequency the same, produces a very similar dynamic response with essentially the same amplitude window for trapped pulsations, $\varepsilon < 2.5$.

Upon comparing the equivalent graphs shown in Figs. 11(b), 11(d), and 11(f) the time duration required for the bubble to reach the wall, in terms of the dimensionless time $t/(2\pi)$ that essentially measures the number of volume pulsations, scales with the square of the amplitude δ_o of radial pulsations during saturation. Shell properties affect the Bjerknes force in Eq. (14) through the amplitude δ_o of the radial pulsation, whereas forcing frequency ω_f is used to make time dimensionless. Nevertheless, when $\varepsilon = 2$ the time required for trapping to be achieved is significantly lower for the largest χ value, $\chi = 0.48\,\mathrm{N/m}$, reflecting a larger speed of approach when a harder shell is interrogated, as can be gleaned by numerically evaluating the speed of the center of mass from the time evolution of P_1 in Figs. 11(b), 11(d), and 11(f). This is contrary to the expected reduction in the amplitude of the radial pulsation for a more rigid shell. The reason for this behavior is illustrated by the volume pulsations depicted in Fig. 11 which are seen to be more intense as the area dilatation increases. Upon calculating the eigenfrequency for volume pulsations of this shell type it turns out that $\omega_0/(2\pi) \approx 0.55$, 0.75, and 1.05 MHz when $\chi = 0.12$, 0.24, and 0.48, respectively. Consequently the latter shell is closer to resonance and this entails larger radial oscillations, i.e., larger amplitude δ_o, and therefore larger translational velocity. As a result, in the latter case the parameter range is close to the threshold for parametric mode excitation and trapping could not be very clearly captured.

Shell deformation and the prolate and oblate shapes obtained during the acceleration and trapped phases of the pulsation are similar in all three cases examined in Fig. 11. During trapped pulsations the bubble shape becomes flattened in the vicinity of the wall with the softer shell, $\chi = 0.12$ N/m, exhibiting a similar flat region with the case for $\chi = 0.24\,\mathrm{N/m}$ despite its smaller resistance to elongation and compression, Figs. 11(a), Fig. 11(c). This is a result of the similar amplitude of volume pulsations in the two cases illustrated in Figs. 11(b) and 11(d). The large amplitude of radial pulsation coupled with the shell properties entering the force deformation relation in Eqs. (19) and (20) also explain the tendency for the harder shell, $\chi = 0.48$ N/m, to develop a larger flattened area as it approaches the wall, Fig. 11(e), despite its larger resistance to elongation and compression. The varying intensity of radial pulsations at saturation δ_o is directly associated with the variation of

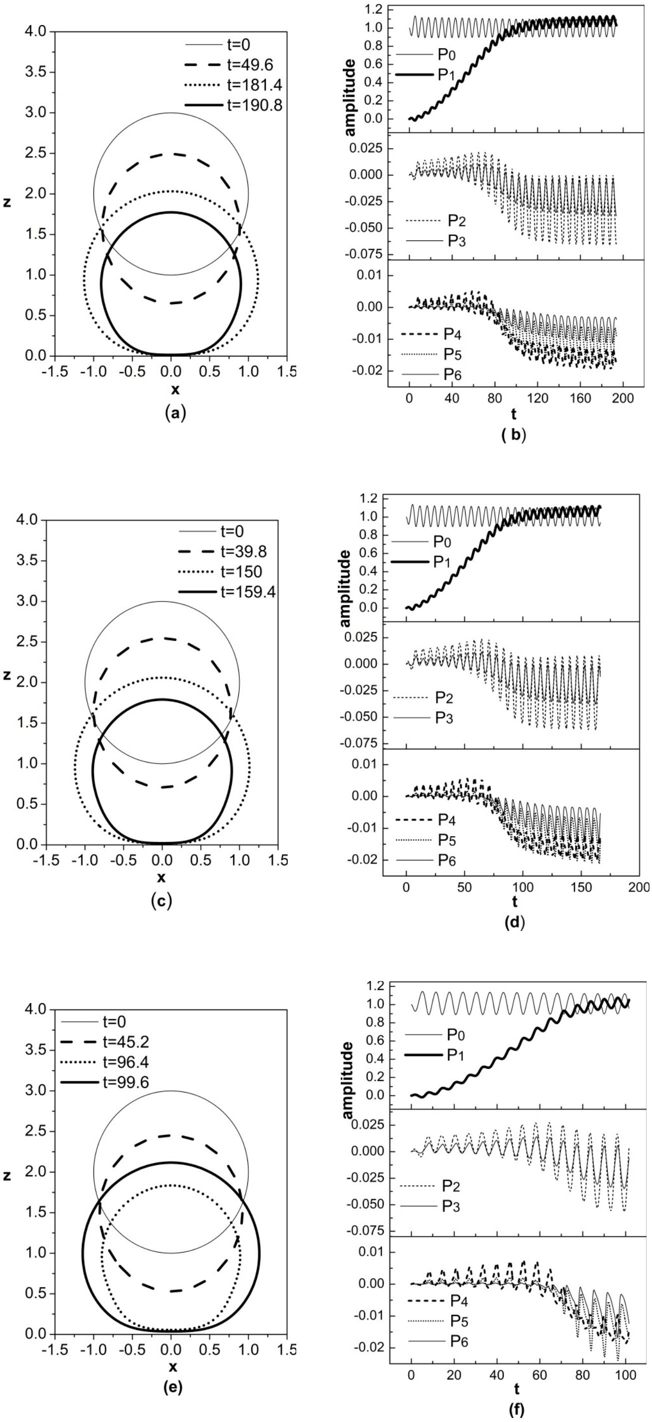

FIG. 11. Temporal evolution of (a),(c),(e) bubble shape and (b),(d),(f) breathing P_0, translational P_1 modes, and shape mode decomposition when the area dilatation modulus χ is set to 0.12, 0.24, and 0.48 N/m, respectively; the initial bubble radius is $R_0 = 3.6\,\mu$m; shell properties are $\mu_s = 120 \times 10^{-9}$ kg/s and $k_B = 3 \times 10^{-14}$ N m; the initial distance from the wall is set to $z_{c0} = 2$; an acoustic disturbance of frequency $f = 1.7$ MHz and amplitude $\varepsilon = 2$ is imposed.

respective resonance frequencies. The one pertaining to $\chi = 0.48$ N/m lies closer to the forcing, as discussed in the previous paragraph, and this reflects in the amplitude δ_o of its radial pulsation and is also evident in the shape of the microbubble as it pulsates in the wall vicinity, that exhibits a longer contact area in the manner described by Eq. (20).

The effect of shell bending resistance on the trapping procedure and its final shape is examined next. To this end, we consider the contrast agent that was acoustically interrogated in Figs. 5 and 7, and we repeat the simulation for two cases with increased bending resistance, $k_B = 6 \times 10^{-14}$ N m and $k_B = 12 \times 10^{-14}$ N m. The numerical results for both cases are presented in Fig. 12 and it is obvious that no significant impact on the translational velocity of the bubble, and therefore on the time needed for the bubble to reach the wall, is observed. This is expected since the amplitude of the radial pulsation as well as the resonance frequency do not depend on the bending resistance of the shell. The evolution of the shape modes is also similar and very close to the pattern that is registered for the bubble with the smaller bending resistance ($k_B = 3 \times 10^{-14}$ N m) shown in Fig. 5. Finally, based on the critical threshold for the onset of parametric mode excitation presented in Table I, the shells that are characterized by higher bending resistance are more stable in that respect and consequently can be trapped for larger sound amplitudes. Indicative profiles of the radial velocity are also shown for the case corresponding to Fig. 12(b), $k_B = 12 \times 10^{-14}$ N m, at maximum translational velocity of the microbubble towards (away from) the wall captured at the time instants of transition from expansion to compression and vice versa, Fig. 12(e) [Fig. 12(f)]. The pattern of mixed shear and pressure driven flow out of and into the gap formed between the shell and wall is recovered in the manner described in the context of Figs. 6 and 7. The pressure driven aspect of the flow is enhanced as the axis of symmetry is approached in comparison with Figs. 7(e) and 7(f), since the gradients in the bending strain are more important, see also Eq. (17), due to the larger bending resistance. At all cases, however, the periodic nature of the oscillating Stokes layer persists in the gap region and no indication of steady streaming was captured in the simulations as expected based on the in phase pulsation of the microbubble volume and center of mass.

Pertaining to the degree of flattening during trapped oscillations as a function of shell properties, Fig. 10(b) is enriched with the relevant points on the $[\Delta/R_0, F_B/(\chi k_B)^{1/2}]$ plane as calculated via the above simulations with varying area dilatation and bending modulus (shown in Figs. 11 and 12) and it is seen that they conform with the Reissner type time-averaged response discussed in the previous subsection. In particular, the degree of flattening and shell deformation agree with the prediction of Eqs. (19), with the length of the contact region decreasing with the square root of area dilatation and bending resistance.

C. Effect of shell viscosity

In order to assess the effect of shell viscosity on the dynamics of bubble motion towards the wall we consider the same contrast agent as in Figs. 4 and 5 while setting shell viscosity to 120×10^{-9} kg/s, i.e., the viscosity used in the simulations depicted in Fig. 11. In this case stability analysis regarding parametric mode excitation predicts P_7 and P_8 as the dominant eigenmodes with an amplitude threshold $\sim$2.5; see also Table I for the amplitude threshold of the major unstable modes. In this context, simulations recover the pattern of trapped pulsations depicted in Figs. 3–9, for the forcing frequency set to 1.7 MHz and the above amplitude range predicted for stability against parametric mode excitation, thus extending the range obtained for a lower shell viscosity. Figures 13(a)–13(d) clearly illustrate this pattern when $\varepsilon = 2$ and 2.2 for the initial distance from the wall set to $z_{c0} = 2$. The same final state of trapped pulsations is obtained for a larger initial distance, e.g., $z_{c0} = 4$, with the time required for the bubble to reach the wall being quadrupled since the speed of the bubble center of mass nearly varies with the inverse distance from the wall, see also Eqs. (14) and (15) and Fig. 8 from paper I, for a relatively small Re_T. In the same context, for fixed initial distance z_{c0}, the force required for trapping the bubble increases with the square of the sound amplitude and so does the speed by which the bubble approaches the wall as the amplitude ε increases. This also reflects in the shape of the microbubble during trapped pulsations,

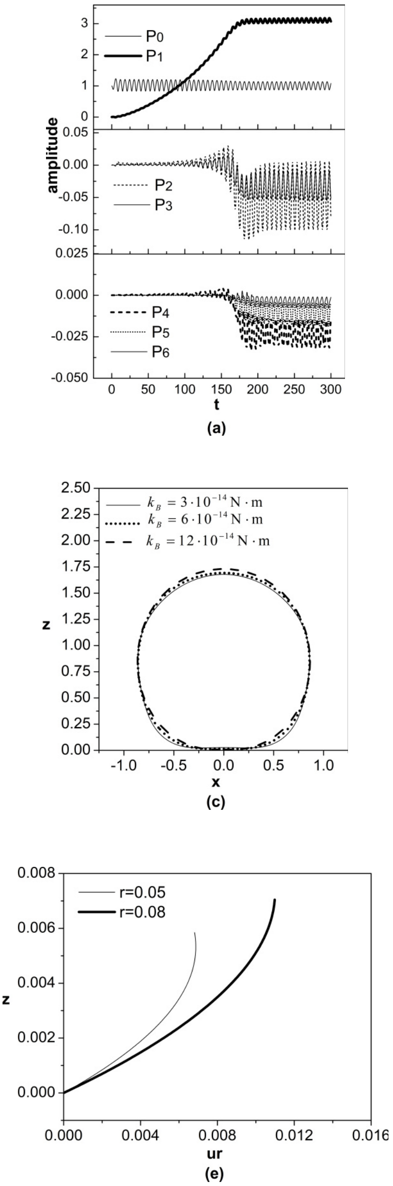

FIG. 12. Temporal evolution of (a),(b) breathing P_0, translational P_1 modes, and shape mode decomposition when the bending resistance is set to $k_B = 6 \times 10^{-14}$ N m and $k_B = 12 \times 10^{-14}$ N m, respectively, (c) bubble shape at maximum compression $t = 285.2$ for the different k_B values, (d) zoom-in of the shape close to the wall at $t = 285.2$, (e),(f) indicative radial velocity profiles below the contact region at the time instants corresponding to transition from expansion to compression and vice versa when $k_B = 12 \times 10^{-14}$ N m; the initial bubble radius is $R_0 = 3.6\,\mu$m; shell properties are $\mu_s = 60 \times 10^{-9}$ kg/s and $\chi = 0.24$ N/m; the initial distance from the wall is set to $z_{c0} = 4$; an acoustic disturbance of frequency $f = 1.7$ MHz and amplitude $\varepsilon = 2$ is imposed.

see Figs. 13(a) and 13(c), that exhibits a gradual elongation around the south pole facing the wall.

Upon averaging during one period of the pulsation we recover the balance between secondary Bjerknes force F_B and lubrication pressure that develops in the contact region of the shell around

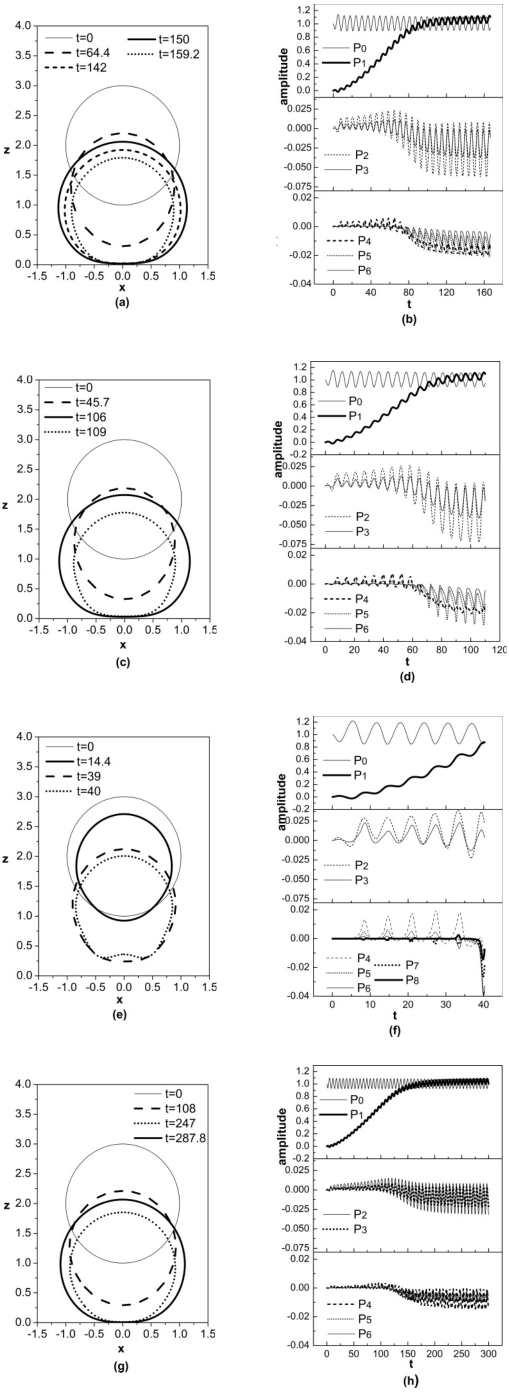

FIG. 13. Temporal evolution of (a),(c),(e) bubble shape and (b),(d),(f) breathing P_0, translational P_1 modes, and shape mode decomposition when $\mu_s = 120 \times 10^{-9}$ kg/s and $\varepsilon = 2$, 2.2, and 3.0, respectively. Temporal evolution of (g) bubble shape and (h) breathing P_0, translational P_1 modes, and shape mode decomposition when $\mu_s = 300 \times 10^{-9}$ kg/s and $\varepsilon = 3$; the initial bubble radius is $R_0 = 3.6\,\mu$m; shell properties are $\chi = 0.24$ N/m and $k_B = 3 \times 10^{-14}$ N m; the initial distance from the wall is set to $z_{c0} = 2$; an acoustic disturbance of frequency $f = 1.7$ MHz is imposed.

its south pole due to variations of the transverse shear q, expressed by Eqs. (19) and (20), once the appropriate amplitude δ_o for the radial pulsation is employed for the calculation of F_B via Eq. (14). In fact, the corresponding points in the $(F_B/\sqrt{k_b\chi}, \Delta/R_0)$ plane obtained by the above described simulations with increased shell viscosity, shown in Figs. 13(a)–13(d), 13(g), and 13(h), fall along the curve shown in Fig. 10(b).

On increasing the amplitude of the external disturbance to $\varepsilon = 3$ for the same forcing frequency $f = 1.7$ MHz we recover the process of dynamic buckling. When the initial bubble distance from the wall is set to $z_{c0} = 4$ the bubble shapes remain almost spherical for the most part of its translation towards the wall and this facilitates growth of the unstable modes P_6, P_7, and P_8 as predicted by stability analysis; see also Table I. At the same time and as the bubble approaches the wall the pattern of energy transfer between the above modes and P_2 and P_3 is also present. However, this process is not sufficient to sustain the integrity of the bubble and simulations have to eventually stop due to growth of high modes. Reducing the initial distance to $z_{c0} = 2$ enhances the process of energy transfer from the higher shape modes to P_2 as the bubble approaches the wall, Fig. 13(f). However, as the bubble starts pulsating in the vicinity of the wall, buckling of the interface takes place that is signified by dimple formation, in order to alleviate elastic stresses that develop on the shell; see also Fig. 13(e). This further destabilizes the shell and the simulations have to stop at the point of maximum volume compression. Increasing shell viscosity to 300×10^{-9} kg/s, for the same initial distance $z_{c0} = 2$, allows for trapped pulsations to be captured for an acoustic disturbance with amplitude $\varepsilon = 3$, as illustrated in Figs. 13(g) and 13(h). This is also in agreement with stability analysis that predicts a similar threshold, $\varepsilon \approx 3.1$, for parametric mode excitation for the set of shell parameters employed in Figs. 13(g) and 13(h); see also Table I. It should be stressed that it is strictly a dynamic divergence effect, or “dynamic buckling,” that instigates the onset of shape modes and destabilizes the process of trapping and this is corroborated by the findings of parametric stability analysis that validate the amplitude threshold for such an effect to arise. In fact, simulations of the static response of a coated microbubble with the same elastic properties as the one that is acoustically interrogated in the present study, subject to a similar static pressure distribution, reveal that buckling does not take place. In particular, as the force increases, static calculations reveal that volume compression instead of bending absorbs the extra energy added to the shell [31] thus allowing formation of a longer flat contact region.

In order to illustrate the effect of shell viscosity on the flow arrangement in the region right below the microbubble, Figs. 14 and 15 contain plots of the elastic stresses and interfacial velocity along the shell-liquid interface, as well as indicative radial velocity profiles for the case depicted in Figs. 13(a) and 13(b). Three time instants during a period of trapped pulsations are selected corresponding to maximum volume expansion, Fig. 14, and the time instants at which volume pulsation acquires maximum speed as the bubble moves from compression to expansion and vice versa, Fig. 15. The latter two time instants are characterized by large positive (negative) normal and tangential velocities, Fig. 15(a) [Fig. 15(b)], that signify departure (approach) of the bubble center of mass with respect to the wall. The tangential and normal velocities along the interface are very small during maximum expansion and compression of the radial motion, hence they are not shown. Nevertheless, the pattern of pressure driven flow moving in and out of the gap between the shell and wall during maximum expansion and compression, illustrated by Fig. 7 for lower shell viscosity, is recovered in this case, e.g., Figs. 14(a)–14(c) pertaining to maximum expansion. In particular, liquid overpressure across the shell interface balances variations in transverse shear q in the flattened contact region, see also Eq. (17) and Figs. 14(a) and 14(b), which, in the absence of significant viscous shell stresses, generate a quadratic velocity profile signifying pressure driven flow out of the gap, Fig. 14(c). The case with maximum compression exhibits a similar behavior as in Fig. 7(d) with the pressure driven flow directed towards the gap, hence it is not shown here in the interest of brevity.

The relative strength of the pressure driven flow as a result of variations in the shear stress resultant on the shell, in comparison with the shear driven flow due to viscous shell stresses, is a key feature of the flow arrangement in the gap region underneath the contact region of the shell. A

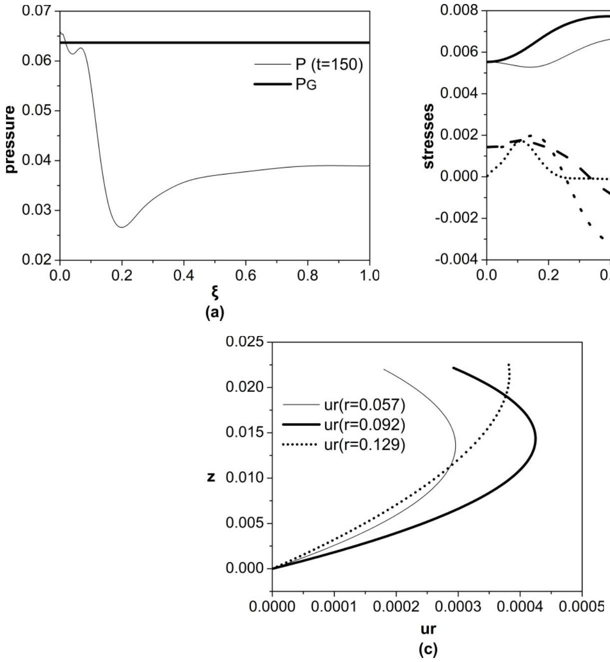

FIG. 14. Interfacial distribution of (a) pressure, (b) viscoelastic stresses, and (c) radial velocity profile during maximum expansion during trapped pulsations; shell properties are $\mu_s = 120 \times 10^{-9}$ kg/s, $\chi = 0.24\,\mathrm{N/m}$ and $k_B = 3 \times 10^{-14}$ N m; the initial bubble radius is $R_0 = 3.6\,\mu$m; the initial distance from the wall is set to $z_{c0} = 2$; an acoustic disturbance of frequency $f = 1.7$ MHz and sound amplitude $\varepsilon = 2$ is imposed.

nearly shear driven flow pattern was captured by the simulations in the transition region between the bulk and contact region of the shell, Figs. 15(c) and 15(d). In fact, at the time instants of transition from compression to expansion and vice versa, pressure drop across the shell-liquid interface is balanced by oscillating viscous stresses in the bulk of the shell which, given the large pressure drop in the equator region, generates a maximum in the oscillating tangential and normal velocities as well, Figs. 15(a) and 15(b). The pressure drop and viscoelastic stress distribution along the interface provided in Figs. 15(e) and 15(f) and Figs. 15(g) and 15(h) illustrate this pattern, also obtained in Figs. 6, 7, and 12. As the flow enters the contact region pressure drop develops due to variations in the shear stress resultant q and this results in a mixed shear and pressure driven flow pattern out of and in the gap during expansion and compression of the microbubble, respectively.

In particular, the flow pattern in the transition region between the flattened region and the bulk of the shell is determined by the balance between viscoelastic shell stresses and viscous shear in the film; see also Figs. 15(g) and 15(h) and Figs. 15(i) and 15(j) showing the stress distribution along the interface due to shell viscoelasticity and liquid viscosity. Viscous shear is maximized in that region as can also be inferred by the tangential velocity distribution, Figs. 15(a) and 15(b). Thus the terms in the tangential force balance scale as

$$\frac{\partial \tau_s}{\partial \hat{s}} + k_s q \approx \frac{1}{\mathrm{Re}}\frac{\partial \hat{u}}{\partial \hat{z}}, \quad \hat{z} \equiv \frac{z'}{\Delta}, \quad \hat{s} \equiv \frac{S'}{\ell}, \quad \hat{r} \equiv \frac{r'}{\ell}, \quad \hat{u}, \hat{u}_s \equiv \frac{u', u'_s}{\omega_f \ell}, \quad \hat{z} = \hat{h}(\hat{r}, t) \equiv \frac{h'}{\Delta} \tag{21}$$

with $\hat{u}$ signifying the scaled radial velocity in this region. Since on average during a period of the pulsation transverse shear and purely elastic strain balance each other, on balancing viscous stresses in the shell and the liquid we obtain an estimate for the film thickness in the contact and transition

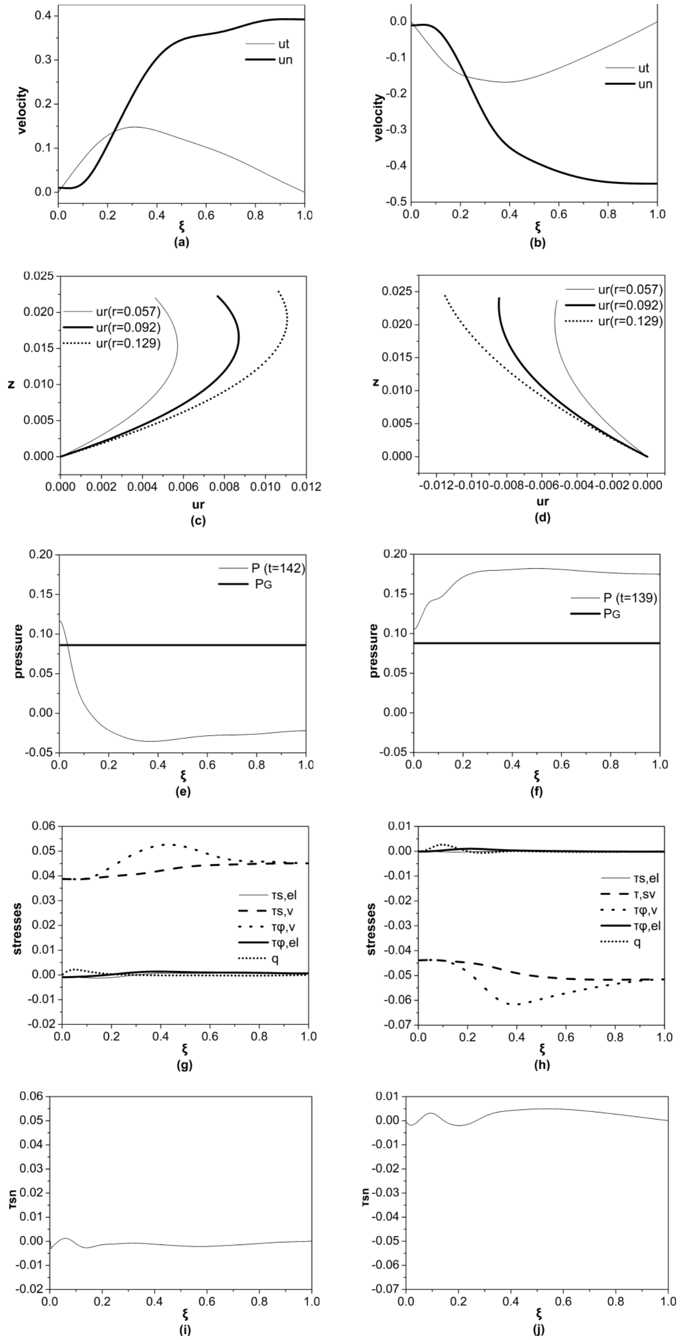

FIG. 15. Interfacial distribution during trapped pulsations of (a),(b) normal and tangential interfacial velocity, (c),(d) radial velocity profiles, (e),(f) interfacial distribution of pressure, (g),(h) interfacial distribution of viscoelastic stresses, and (i),(j) interfacial distribution of liquid tangential stresses, when the volume pulsation crosses from compression to expansion and from expansion to compression, respectively; the initial bubble radius is $R_0 = 3.6\,\mu\text{m}$; shell properties $\mu_s = 120 \times 10^{-9}\,\text{kg/s}$, $\chi = 0.24\,\text{N/m}$ and $k_B = 3 \times 10^{-14}\,\text{N m}$; the initial distance from the wall is set to $z_{c0} = 2$; an acoustic disturbance of frequency $f = 1.7$ MHz and sound amplitude $\varepsilon = 2$ is imposed.

regions,

$$\frac{1}{\mathrm{Re_s}}\frac{\partial^2 \hat{u}_s}{\partial \hat{s}^2}+\frac{\partial \tau_{s,\mathrm{el}}}{\partial \hat{s}}+k_s q \approx \frac{1}{\mathrm{Re}}\frac{\partial \hat{u}}{\partial \hat{z}} \xrightarrow{\frac{\partial \tau_{s,\mathrm{el}}}{\partial \hat{s}}\sim k_s q} \frac{\mathrm{Re_s}}{\mathrm{Re}}\frac{\partial \hat{u}}{\partial \hat{z}} \approx \frac{\partial^2 \hat{u}_s}{\partial \hat{s}^2} \to \frac{\partial \hat{u}}{\partial \bar{z}} = O(1),$$

$$\bar{z} = \hat{z}\frac{\mathrm{Re}}{\mathrm{Re_s}} = \hat{z}\frac{\mu_s}{\mu R_0}, \tag{22a}$$

$$\bar{h} = \hat{h}\frac{\mu_s}{\mu R_0} = O(1) \to h' \approx R_0\frac{\mu R_0}{\mu_s}\frac{\Delta}{R_0}$$

$$= R_0\frac{\mu R_0}{\mu_s}\frac{2\pi\delta_o^2}{C}\left(\frac{R_0}{4R_0}\right)^2\sqrt{\frac{\rho\omega_f^2 R_0^5}{k_B}}\sqrt{\frac{\rho\omega_f^2 R_0^3}{\chi}}; \tag{22b}$$

in the above relation $\hat{u}_s$ denotes the tangential velocity of the shell along the interface with constant C bearing the significance ascribed to it in Eq. (20). Upon introducing indicative values of the natural and geometric parameters involved in the above scaling we obtain an estimate for the length scale of the film thickness that is on the order of 20–50 nm, which conforms with the calculated gap between the shell and rigid wall underneath the south pole, averaged over a period of trapped oscillation. In the context of the situations presented herein the above pattern is manifested in the increased viscous shell stresses and smaller film thickness as shell viscosity increases. When the shell viscosity is smaller, Figs. 5 and 7, the amplitude of the radial motion δ_o is larger, and consequently the tangential velocity of the shell-fluid interface is larger and this is manifested in the oscillatory, yet more intense, shear driven type flow that is exhibited in the gap region beneath the south pole. This can also be verified by inspection and comparison of the radial velocity profiles obtained in the flattened region of the shell shown in Figs. 7(e) and 7(f), Figs. 12(e) and 12(f), and Figs. 15(c) and 15(d).

Clearly the above trends will also be affected by the relative importance of the three shell stiffnesses, i.e., between area dilatation, bending resistance, and shell viscosity, $\chi/(\mu_s\omega_f)$, $k_B/(\mu_s\omega_f R_0^2)$. In fact, for relatively small k_B, $k_B/(\mu\omega_f R_0^3) \ll 1$, the strength of the Poiseuille flow is weak and the flow in the contact region is essentially that of an oscillating Stokes layer with zero average velocity, Fig. 7. As shell viscosity decreases or bending resistance increases the pressure driven flow due to variations in the transverse shear q becomes more important and is captured in the radial velocity profile, as in Figs. 12(e) and 12(f). However, a more accurate asymptotic analysis is required to corroborate the above findings and is left for a future study. Nevertheless, no average acoustic streaming component was observed in the simulations performed in the present study since the streaming Reynolds was small and the radial and translational oscillations remained in phase [13].

The above flow arrangement is similar to the response pattern obtained for liquid drops that approach each other at constant speed when they are dispersed in another viscous liquid [35,36], where interfacial mobility plays an important role in film drainage and stability. In particular, when a surfactant laden drop is investigated [36], the effective elasticity of the interface that results due to the variation of surface tension prevents dimple formation thus favoring elongation. The drop interface forms a dimple pointing towards the drop interior when the lubrication overpressure in the region between the two colliding drops exceeds a certain threshold. In the present study it is shell viscosity and area dilatation that control the extent of interfacial mobility and the resulting contact length during trapped pulsation, whereas bending resistance allows for bending and compression in the presence of external overpressures thus preventing buckling and breakup at relatively large pressure amplitudes.

V. CONCLUSIONS

In the present study we numerically investigate the dynamic response of an encapsulated microbubble in a wall restricted flow due to an acoustic disturbance in the far pressure field, when viscous and inertia forces in the surrounding fluid and viscoelastic stresses in the protective shell are accounted for. Coupling a superparametric finite element methodology with an elliptic mesh generation scheme [19,20] allowed us to capture the dynamic response of coated microbubbles until trapping is achieved in the form of a steady pulsation at a very low average distance from the wall.

The bubble is seen to perform volume pulsations while translating towards the wall due to the secondary Bjerknes force with a velocity that is produced by the almost instantaneous equilibrium between Bjerknes forces and viscous drag from the surrounding liquid [20,33]. Provided we remain below the threshold for parametric shape mode excitation to take place, the microbubble accelerates and eventually reaches the wall where its motion is halted due to the onset of elastolubrication pressure that provides the reaction to the Bjerknes force. It arises in the nearly flat contact region beneath the south pole of the bubble and forces the shell to compress and bend. The integral of the lubrication pressure along the contact region is counteracted by the local reaction forces due to the internal gas pressure in the contact region, the transverse shear stress resultant at the edge of the contact region, and surface tension due to the bulk of the shell; see also the schematic provided in Fig. 10(a) and the balance in Eq. (18). On averaging over a period of the forcing the force that counteracts the secondary Bjerknes force and produces trapped pulsations at a very small distance from the wall is obtained. It is a Reissner [34] type force balance, complemented with the additional shell stiffness due to gas compressibility and surface tension, that produces deformation and a contact length in the nearly flat region around the south pole, as a function of shell bending, area dilatation modulus, and interfacial tension. In the limit of small deformations, $\Delta \ll R_0$, the expression $F_B/\sqrt{\chi k_B} \sim 8(\Delta/R_0) + 2.5\pi\sqrt{\sigma^2 R_0^2/(\chi k_B)}(\Delta/R_0)^{3/2}$ describes the force balance that is satisfied by the numerically obtained force vs deformation curve, Fig. 10, as the shell and acoustic disturbance parameters vary. The reduction in contact length with increasing bending and area dilatation moduli is captured by Eq. (20) that is obtained by introducing the expression for Bjerknes force, Eq. (14), in the above force deformation law.

During trapped pulsations away from the wall pressure drop across the shell is balanced by surface tension along with elongational (compressive) elastic stresses when the bubble achieves maximum (minimum) volume, and by elongational (compressive) viscous elastic stresses during the expansion (contraction) phase of the pulsation at which the shell velocity is maximized. In particular, when it achieves maximum expansion a local pressure minimum arises in the liquid in the equator region, towards which fluid leaving the two poles is directed. Consequently maximum tensile stresses are achieved at the equator region that are manifested in the oblate shape acquired by the microbubble as it pulsates in the vicinity of the wall. This type of asymmetric pulsation occurring perpendicular to the wall between prolate and oblate shapes has also been reported experimentally [8], indicating a major wall effect that is robustly reproduced by the present simulation.

The fluid motion during trapped pulsations is oscillatory and no acoustic streaming component was captured during the simulations since the translational and volume pulsations are in phase [13]. In fact, immediately after the shell volume pulsation acquires maximum positive (negative) speed the center of mass translates away (towards) the rigid wall. In the thin film that occupies the region between the flattened shell and rigid wall the flow pattern is a combination of an oscillatory pressure driven flow, due to pressure variations that arise as a result of variations in the transverse shear stress resultant on the shell, and an oscillatory Stokes layer due to the tangential velocity of the mobile shell-liquid interface. They are both averaged to zero over the period of the forcing with the pressure driven flow being present in the contact region throughout the pulsation, and the shear flow mainly in the transition region that joins the bulk of the shell with the contact region. The tangential force balance in the latter region provides an estimate for the film thickness, Eqs. (22a) and (22b), where the parameter $\mu_s/(\mu R_0)$ that controls the balance between viscous shell and liquid stresses is introduced in the estimate. In this fashion film thicknesses that are on the order of tens of nm's are predicted, in agreement with the simulations, and very large instantaneous values of wall shear that are on the order of 10^4 and 10^5 $\mathrm{N/m^2}$.

A parametric study was also conducted in order to examine the influence of the shell viscoelastic properties and acoustic excitation characteristics on the above described dynamic response pattern. It was thus demonstrated that increasing shell viscosity and forcing frequency has a beneficial effect in the trapping procedure as it extends the acceptable range in sound amplitude for stable pulsations without excessive growth of shape modes, by reducing the amplitude of volume pulsation. At the same time, however, it is of great importance to accurately calculate the strength of instantaneous wall shear and to assess the possibility, and relevant parameter range, for the onset of acoustic microstreaming [6,7,13,14], depending also on the shell viscoelastic behavior. Proper choice of the latter shell properties, the configuration of the flow domain, and the resulting length and degree of flatness of the contact region, will lead to optimal conditions pertaining to the intensity and duration of the emerging wall shear and play an important role in the design and optimization of novel biomedical processes such as sonoporation and contrast assisted drug delivery.

ACKNOWLEDGMENTS

This research has been carried out within the framework of the invitation "Expression of interest for holders of doctoral diploma, for scholarship for postdoctoral research" of the University of Thessaly which is implemented by the University of Thessaly and is funded by the Stavros Niarchos Foundation.

---

[1] B. A. Kaufmann, K. Wei, and J. R. Lindner, Contrast echocardiography, Curr. Probl. Cardiol. **32**, 51 (2007).

[2] K. Efthymiou, N. Pelekasis, M. B. Butler, D. H. Thomas, and V. Sboros, The effect of resonance on transient microbubble acoustic response: Experimental observations and numerical simulations, J. Acoust. Soc. Am. **143**, 1392 (2018).

[3] K. Ferrara, R. Pollard, and M. Borden, Ultrasound microbubble contrast agents: fundamentals and application to gene and drug delivery, Ann. Rev. Biomed. Eng. **9**, 415 (2007).

[4] Y. Taniyama, K. Tachibana, K. Hiraoka, T. Namba, K. Yamasaki, N. Hashiya, M. Aoki, T. Ogihara, K. Yasufumi, and R. Morishita, Local delivery of plasmid DNA into rat carotid artery using ultrasound, Circulation **105**, 1233 (2002).

[5] A. A. Doinikov and A. Bouakaz, Acoustic microstreaming around an encapsulated particle, J. Acoust. Soc. Am. **127**, 1218 (2010).

[6] P. Marmottant and S. Hilgenfeldt, Controlled vesicle deformation and lysis by single oscillating bubbles, Nature (London) **423**, 153 (2003).

[7] A. A. Doinikov and A. Bouakaz, Effect of a distant rigid wall on microstreaming generated by an acoustically driven gas bubble, J. Fluid Mech. **742**, 425 (2014).

[8] H. J. Vos, B. Dollet, J. G. Bosch, M. Versluis, and N. de Jong, Nonspherical vibrations of microbubbles in contact with a wall - A pilot study at low mechanical index, Ultrasound Med. Biol. **34**, 685 (2008).

[9] H. Chen, W. Kreider, A. A. Brayman, M. R. Bailey, and T. J. Matula, Blood Vessel Deformations on Microsecond Time Scales by Ultrasonic Cavitation, Phys. Rev. Lett. **106**, 034301 (2011).

[10] S. Zhao, K. W. Ferrara, and P. A. Dayton, Asymmetric oscillation of adherent targeted ultrasound contrast agents, Appl. Phys. Lett. **87**, 134103 (2005).

[11] V. Garbin, M. Overvelde, B. Dollet, N. de Jong, D. Loshe, and M. Versluis, Unbinding of targeted ultrasound contrast agent microbubbles by secondary acoustic forces, Phys. Med. Biol. **56**, 6161 (2011).

[12] T. Kokhuis, V. Garbin, K. Kooiman, B. Naaijkens, L. Juffermans, O. Kamp, A. Van der Steen, M. Versluis, and N. de Jong, Secondary Bjerknes forces deform targeted microbubbles, Ultrasound Med. Biol. **39**, 490 (2013).

[13] M. S. Longuet-Higgins, Viscous streaming from an oscillating spherical bubble, Proc. R. Soc. London **454**, 725 (1998).

[14] N. Mobadersany and K. Sarkar, Acoustic microstreaming near a plane wall due to a pulsating free or coated bubble: velocity, vorticity and closed streamlines, J. Fluid Mech. **875**, 781 (2019).

[15] K. Tsiglifis and N. Pelekasis, Simulations of insonated contrast agents: Saturation and transient break-up, Phys. Fluids **25**, 032109 (2013).

[16] S. Qin and K. W. Ferrara, Acoustic response of compliable microvessels containing ultrasound contrast agents, Phys. Med. Biol. **51**, 5065 (2006).

[17] Y. Liu, K. Sugiyama, S. Takagi, and Y. Matsumoto, Numerical study on the shape oscillation of an encapsulated microbubble in ultrasound field, Phys. Fluids **23**, 041904 (2011).

[18] K. Tsiglifis and N. Pelekasis, Parametric stability and dynamic buckling of encapsulated microbubble subject to acoustic disturbances, Phys. Fluids **23**, 012102 (2011).

[19] M. Vlachomitrou and N. Pelekasis, Dynamic simulation of a coated microbubble in an unbounded flow: response to a step change in pressure, J. Fluid Mech. **822**, 717 (2017).

[20] M. Vlachomitrou and N. Pelekasis, Numerical study of the interaction between a pulsating contrast agent and a rigid wall, part I: Translational motion, Phys. Rev. Fluids **5**, 123606 (2020).

[21] K. Tsiglifis and N. Pelekasis, Nonlinear radial oscillations of encapsulated microbubbles subject to ultrasound: the effect of membrane constitutive law, J. Acoust. Soc. Am. **123**, 4059 (2008).

[22] D. B. Khismatullin and A. Nadim, Radial oscillations of encapsulated microbubbles in viscoelastic liquids, Phys. Fluids **14**, 3534 (2002).

[23] K. Sarkar, W. T. Shi, D. Chatterjee, and F. Forsberg, Characterization of ultrasound contrast microbubbles using *in vitro* experiments and viscous and viscoelastic interface models for encapsulation, J. Acoust. Soc. Am. **118**, 539 (2005).

[24] P. Marmottant, S. Van der Meer, M. Emmer, M. Versluis, N. de Jong, S. Hilgenfeldt, and D. Lohse, A model for large amplitude oscillations of coated bubbles accounting for buckling and rupture, J. Acoust. Soc. Am. **118**, 3499 (2005).

[25] P. Timoshenko and S. Woinowsky-Krieger, *Theory of Plates and Shells* (McGraw-Hill, Singapore, 1959).

[26] C. Pozrikidis, Effect of membrane bending stiffness on the deformation of capsules in simple shear flow, J. Fluid Mech. **440**, 269 (2001).

[27] D. Barthes-Biesel, A. Diaz, and E. Dhenin, Effect of constitutive laws for two-dimensional membranes on flow-induced capsule deformation, J. Fluid Mech. **460**, 211 (2002).

[28] K. N. Christodoulou and L. E. Scriven, Discretization of free surface flows and other moving boundary problems, J. Comput. Phys. **99**, 39 (1992).

[29] K. Tsiveriotis and R. A. Brown, Boundary-conforming mapping applied to computations of highly deformed solidification interfaces, Int. J. Numer. Methods Fluids **14**, 981 (1992).

[30] Y. Dimakopoulos and J. Tsamopoulos, A quasi-elliptic transformation for moving boundary problems with large anisotropic deformations, J. Comput. Phys. **192**, 494 (2003).

[31] A. Lytra and N. Pelekasis, Static response of coated microbubbles compressed between rigid plates: Simulations and asymptotic analysis including elastic and adhesive forces, Phys. Fluids **30**, 030711 (2018).

[32] R. Clift, J. R. Grace, and M. E. Weber, *Bubbles, Drops and Particles* (Academic, New York, 1978).

[33] R. Mei, Flow due to an oscillating sphere and an expression for unsteady drag on the sphere at finite Reynolds number, J. Fluid Mech. **270**, 133 (1994).

[34] E. Reissner, Stresses and small displacements of shallow spherical shells II, J. Math. Phys. **25**, 279 (1946).

[35] E. Klaseboer, J. Ph. Chevaillier, C. Gourdon, and O. Masbernat, Film drainage between colliding drops at constant approach velocity: Experiments and modelling, J. Colloid Interface Sci. **229**, 274 (2000).

[36] L. Y. Yeo, O. K. Matar, E. S. P. de Ortiz, and G. F. Hewitt, Film drainage between two surfactant-coated drops colliding at constant approach velocity, J. Colloid Interface Sci. **257**, 93 (2003).